Cell Reports

Cryo-EM structures of SARS-CoV-2 Omicron BA.2 spike

Graphical abstract

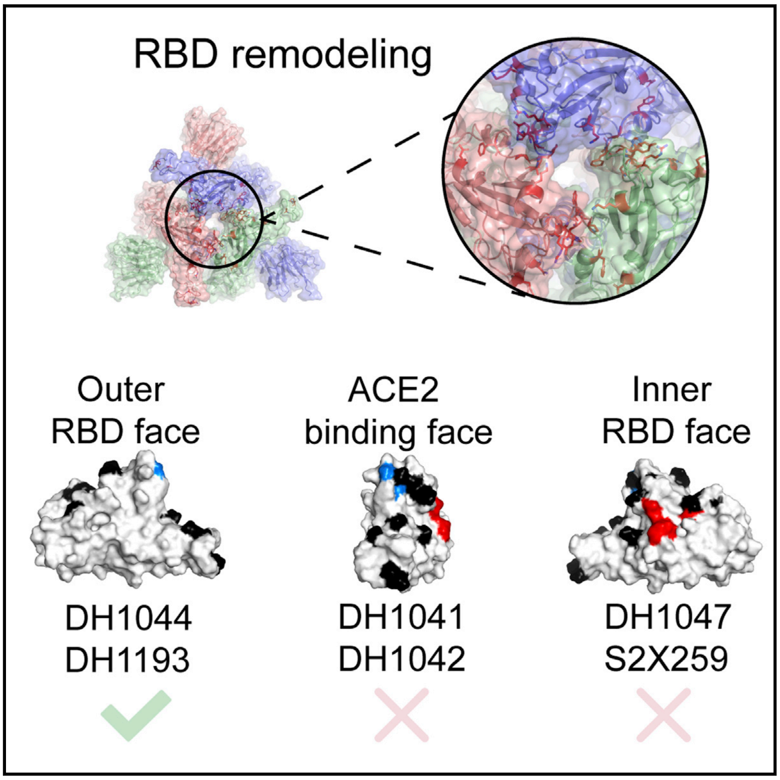

Highlights

- Omicron BA.2 spike (S) protein architecture differs from BA.1 S
- Mutation-induced remodeling of interfacial loops results in more stable BA.2 RBD
- Remodeled BA.2 RBD shows better interprotomer packing in 3-RBD-down (or closed) S
- Fusion peptide in BA.2 S protein is less accessible to antibodies than in BA.1

Authors

Victoria Stalls, Jared Lindenberger, Sophie M.-C. Gobeil, ..., Kevin Wiehe, Barton F. Haynes, Priyamvada Acharya

Correspondence

barton.haynes@duke.edu (B.F.H.),
priyamvada.acharya@duke.edu (P.A.)

In brief

Stalls et al. determine Omicron BA.2 S structures indicating remodeled RBD loops leading to a more thermostable RBD that is better packed within the 3-RBD-down spike and loss of class 4 RBD directed antibody binding. Enhanced spike stability and immune evasion may contribute to BA.2 efficiently outcompeting BA.1.

Stalls et al., 2022, Cell Reports *39*, 111009
June 28, 2022 © 2022 The Author(s).
https://doi.org/10.1016/j.celrep.2022.111009

Cell Reports

CellPress
OPEN ACCESS

Article

Cryo-EM structures of SARS-CoV-2 Omicron BA.2 spike

Victoria Stalls,[1] Jared Lindenberger,[1] Sophie M.-C. Gobeil,[1] Rory Henderson,[1,2] Rob Parks,[1] Maggie Barr,[1] Margaret Deyton,[1] Mitchell Martin,[1] Katarzyna Janowska,[1] Xiao Huang,[1] Aaron May,[1,3] Micah Speakman,[1] Esther Beaudoin,[1] Bryan Kraft,[2] Xiaozhi Lu,[1] Robert J. Edwards,[1,2] Amanda Eaton,[1] David C. Montefiori,[1,4] Wilton B. Williams,[1,3] Kevin O. Saunders,[1,4] Kevin Wiehe,[1,2] Barton F. Haynes,[1,2,5,*] and Priyamvada Acharya[1,3,4,6,*]

[1]Duke Human Vaccine Institute, Durham, NC 27710, USA
[2]Department of Medicine, Duke University, Durham, NC 27710, USA
[3]Department of Biochemistry, Duke University, Durham, NC 27710, USA
[4]Department of Surgery, Duke University, Durham, NC 27710, USA
[5]Department of Immunology, Duke University, Durham, NC 27710, USA
[6]Lead contact
*Correspondence: barton.haynes@duke.edu (B.F.H.), priyamvada.acharya@duke.edu (P.A.)

https://doi.org/10.1016/j.celrep.2022.111009

SUMMARY

The severe acute respiratory syndrome coronavirus 2 (SARS-CoV-2) Omicron BA.2 sub-lineage has gained in proportion relative to BA.1. Because spike (S) protein variations may underlie differences in their pathobiology, here we determine cryoelectron microscopy (cryo-EM) structures of the BA.2 S ectodomain and compare these with previously determined BA.1 S structures. BA.2 receptor-binding domain (RBD) mutations induce remodeling of the RBD structure, resulting in tighter packing and improved thermostability. Interprotomer RBD interactions are enhanced in the closed (or 3-RBD-down) BA.2 S, while the fusion peptide is less accessible to antibodies than in BA.1. Binding and pseudovirus neutralization assays reveal extensive immune evasion while defining epitopes of two outer RBD face-binding antibodies, DH1044 and DH1193, that neutralize both BA.1 and BA.2. Taken together, our results indicate that stabilization of the closed state through interprotomer RBD-RBD packing is a hallmark of the Omicron variant and show differences in key functional regions in the BA.1 and BA.2 S proteins.

INTRODUCTION

The severe acute respiratory syndrome coronavirus 2 (SARS-CoV-2) Omicron B.1.1.529 (or Nextstrain 21M) variant, first detected in November 2021, includes several sub-lineages, including BA.1 (B.1.1.529.1 or Nextstrain clade 21K), BA.2 (B.1.1.529.2 or Nextstrain clade 21L), and BA.3 (B.1.1.529.3 or Nextstrain clade 21M) (Figure 1; Data S1; Hadfield et al., 2018; Sagulenko et al., 2018). BA.1 was the first of the Omicron sub-lineages to rapidly spread worldwide. Subsequently, the proportion of reported BA.2 sequences increased relative to BA.1, with BA.2 overtaking BA.1 to become the dominant coronavirus variant in the United States (https://covid.cdc.gov/covid-data-tracker/#variant-proportions; Viana et al., 2022). The Omicron variant is characterized by its high number of mutations in the spike (S) protein. BA.1 and BA.2 have 20 S protein mutations in common (relative to the D614G S), although they each have 13 and 8 unique mutations, respectively. These differences may be responsible for differences in S-protein-mediated properties, such as host cell entry, viral transmission, and immune recognition.

The BA.1 and BA.2 S proteins differ substantially in their N-terminal domains (NTDs), with only the G142D substitution shared between the two (https://www.gisaid.org/hcov19-variants/; Figure 1A). The G142D substitution also occurred in Delta variant of concern (VOC) sub-lineages and has been associated with immune evasion and high viral loads (Shen et al., 2021). Notably, the BA.2 S protein NTD lacks the H69-V70 deletion (ΔH69-V70) that is present in BA.1, as well as in the Alpha (B.1.1.7) and a mink-associated (ΔFV) variant (Gobeil et al., 2021b; Meng et al., 2021). The BA.2 NTD also lacks the deletion of residues 143–145 and the insertion of three residues at position 214. The receptor-binding domains (RBDs) of BA.1 and BA.2 are more similar with 12 shared mutations, including two, S373P and S375F, that occur in an RBD loop previously implicated in mediating RBD-RBD packing in the 3-RBD-down BA.1 S protein (Gobeil et al., 2022). Residue S371, also part of this interfacial RBD loop, is mutated to Leu in BA.1 or to Phe in BA.2. The Omicron BA.2 S protein harbors an additional amino acid substitution, T376A, within this interfacial loop. RBD mutations that occur in the BA.2 S protein, but not in BA.1, are T376A, D405N, and R408S, whereas G446S and G496S occur in BA.1, but not in the BA.2 S protein. The BA.2 S protein lacks the SD1 T457K and S2 N856K and L981F substitutions that occur in BA.1. All other mutations outside the RBD and NTD region are conserved between the two (Figure 1A).

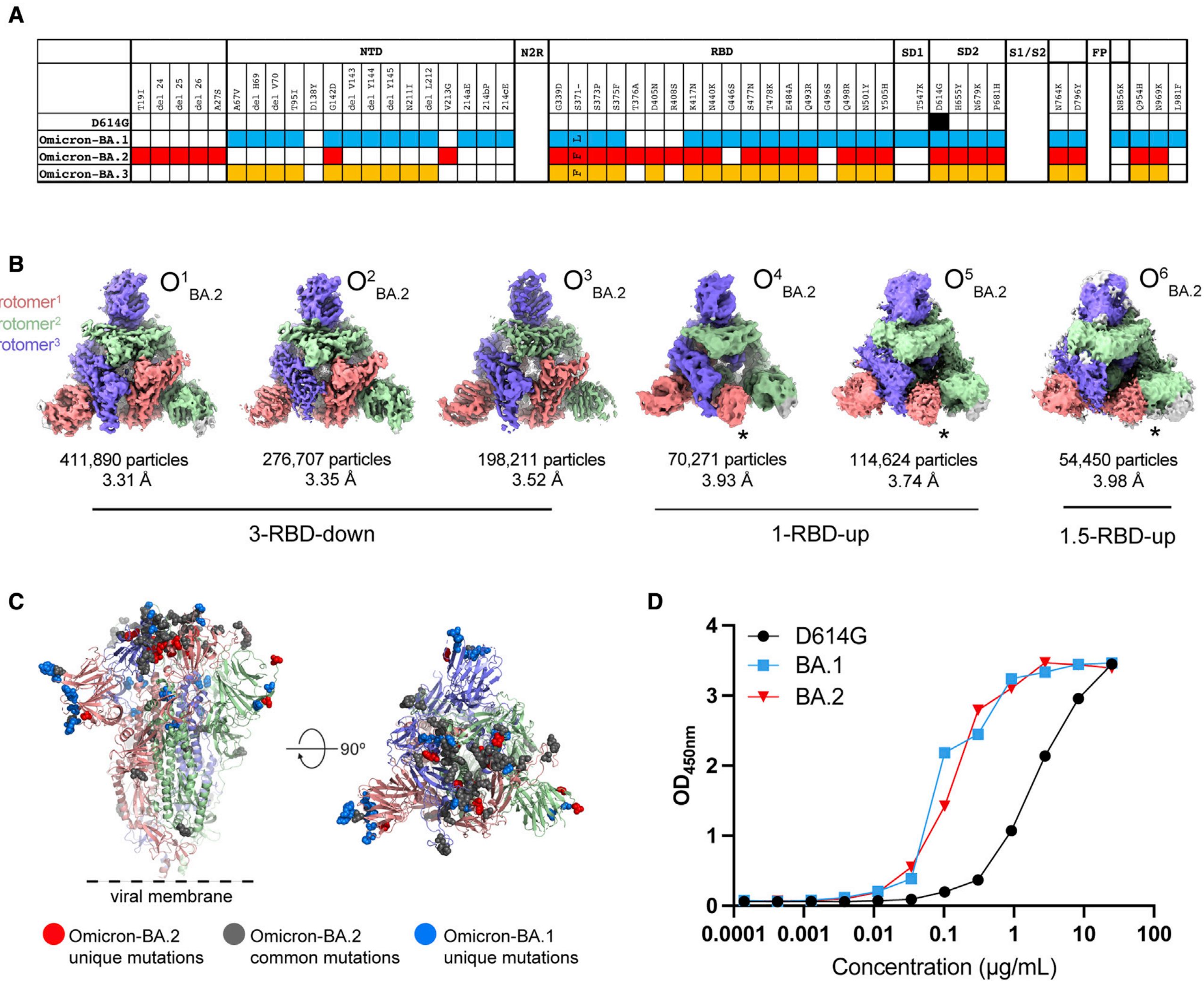

						NTD															N2R	RBD																		SD1	SD2				S1/S2			FP				
	T19I	del 24	del 25	del 26	A27S	A67V	del H69	del V70	T95I	D138Y	G142D	del V143	del Y144	del Y145	N211I	del L212	V213G	214aE	214bP	214cE		G339D	S371-	S373P	S375F	T376A	D405N	R408S	K417N	N440K	G446S	S477N	T478K	E484A	Q493R	G496S	Q498R	N501Y	Y505H	T547K	D614G	H655Y	N679K	P681H		N764K	D796Y		N856K	Q954H	N969K	L981F
D614G																																									⬛											
Omicron-BA.1						🟦	🟦	🟦	🟦		🟦	🟦	🟦	🟦	🟦	🟦		🟦	🟦	🟦		🟦	🟦 L	🟦	🟦				🟦	🟦	🟦	🟦	🟦	🟦	🟦	🟦	🟦	🟦	🟦	🟦	🟦	🟦	🟦	🟦		🟦	🟦		🟦	🟦	🟦	🟦
Omicron-BA.2	🟥	🟥	🟥	🟥	🟥						🟥						🟥					🟥	🟥 F	🟥	🟥	🟥	🟥	🟥	🟥	🟥		🟥	🟥	🟥	🟥		🟥	🟥	🟥		🟥	🟥	🟥	🟥		🟥	🟥			🟥	🟥	
Omicron-BA.3						🟨	🟨	🟨	🟨		🟨	🟨	🟨	🟨	🟨	🟨						🟨	🟨 F	🟨	🟨		🟨		🟨	🟨	🟨	🟨	🟨	🟨	🟨		🟨	🟨	🟨		🟨	🟨	🟨	🟨		🟨	🟨			🟨	🟨	

Figure 1. Structural characterization of SARS-CoV-2 Omicron-BA.2 spike (S) protein

(A) Comparison of residue changes in the S ectodomain (S-GSAS) of SARS-CoV-2 D614G and Omicron variant sub-lineages. Residue changes from the original Wuhan strain are color coded for the variants: D614G (black), BA.1 (blue), BA.2 (red), and BA.3 (yellow).

(B) cryo-EM reconstructions of Omicron-BA.2 S protein 3-RBD-down ($O^1_{BA.2}$: EMD: 26433, PDB: 7UB0; $O^2_{BA.2}$: EMD: 26435, PDB: 7UB5; $O^3_{BA.2}$: EMD: 26436, PDB: 7UB6), 1-RBD-up ($O^4_{BA.2}$: EMD: 26644, $O^5_{BA.2}$: EMD: 26647), and 1.5-RBD-up ($O^6_{BA.2}$: EMD: 26643) states, colored by protomer, and viewed from the host cell membrane. In the RBD-up reconstructions, the "up" RBD is indicated by an asterisk (*).

(C) Omicron-BA.2 S 3-RBD-down structure ($O^1_{BA.2}$: EMD: 26433; PDB: 7UB0) colored by protomer, with common mutations shown as gray spheres, BA.2 unique mutations colored red, and BA.1 unique mutations colored blue.

(D) ACE-2 binding to SARS-CoV-2 S proteins measured by ELISA. OD_{450nm}, optical density 450 nm.

See also Figures S1–S4 and Table S1.

We and others have described structures of the Omicron BA.1 S (Zhou et al., 2022; Mannar et al., 2022; Cerutti et al., 2022; Cui et al., 2022; McCallum et al., 2022; Ye et al., 2022; Gobeil et al., 2022; Zhang et al., 2022). To understand the differences between the BA.1 and BA.2 S proteins, here, we determine cryoelectron microscopy (cryo-EM) structures of the BA.2 S protein ectodomain. The BA.2 S cryo-EM dataset was dominated by 3-RBD-down populations, although we also resolved RBD "up" populations. The dominance of the 3-RBD-down state was driven by improved RBD-RBD packing. An RBD interfacial loop, containing the S373P and S375F residue substitutions, that we had previously identified in the BA.1 S protein as a facilitator of RBD-RBD packing in the 3-RBD-down state (Gobeil et al., 2022) incorporates additional residue substitutions in the BA.2 S protein that drove even closer interactions between the RBDs in the 3-RBD-down structures. These additional mutations also bolstered internal packing within each RBD, resulting in a more stable fold relative to the BA.1 RBD. We found differences in the S2 subunit between the BA.1 and BA.2 S proteins, including reduced accessibility of the fusion peptide (FP) in BA.2 to FP-directed antibodies. While we observed extensive immune evasion, two antibodies, DH1044

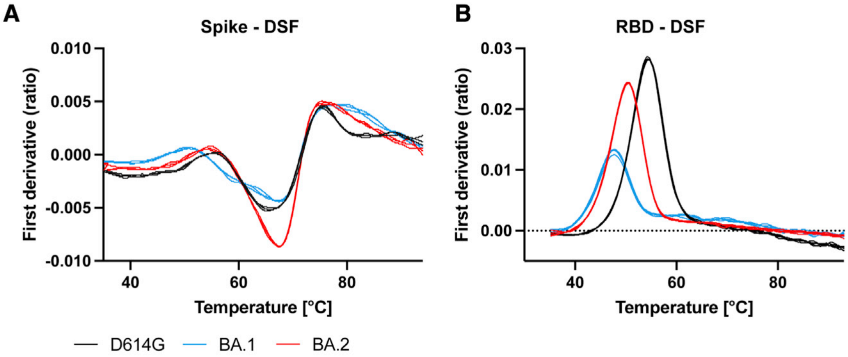

	Ti#1 Mean ± St Dev	Ti#2 Mean ± St Dev	Ti#3 Mean ± St Dev
D614G	55.5 ± 0.4	65.9 ± 0.7	75.5 ± 0.2
Omicron-BA.1	50.8 ± 0.2	67.4 ± 0.2	77.0 ± 0.9
Omicron-BA.2	54.5 ± 0.4	67.5 ± 0.1	76 ± 0.8

	Ti#1 Mean ± St Dev
WT_RBD	54.4 ± 0.1
Omicron-BA.1_RBD	47.7 ± 0.1
Omicron-BA.2_RBD	50.4 ± 0.1

Figure 2. Thermostability of SARS-CoV-2 S ectodomain and RBD

(A) (Top) DSF profiles of the SARS-CoV-2 S ectodomains showing changes in protein intrinsic fluorescence (expressed as the first derivative of the ratio between fluorescence at 350 and 330 nm) with temperature. For each S protein construct, three overlaid curves (technical replicates) are shown. (Bottom) Maxima and minima indicate inflection temperatures, T_i nos. 1–3 (T_i#1, T_i#2, and T_i#3) are represented as mean ± standard deviation from three technical replicates.

(B) Same as (A) but for a monomeric RBD construct.

See also Figures S2 and S9.

and DH1193, bound the outer face of the RBD and neutralized BA.1 and BA.2 in pseudovirus neutralization assays. Taken together, our results demonstrate key differences in the Omicron BA.2 S protein architecture compared with BA.1 that may drive the differences in their biological properties.

RESULTS

Structural diversity and ACE2 binding of the SARS-CoV-2 Omicron BA.2 S protein

We determined cryo-EM structures of the BA.2 S ectodomain using our previously described S-GSAS-D614G platform (Figures 1 and S1–S4; Data S2 and S3; Table S1; Gobeil et al., 2021a, 2021b, 2022). We identified 3-RBD-down S populations (closed; $O^{1}_{BA.2}$, $O^{2}_{BA.2}$, and $O^{3}_{BA.2}$) as well as S populations with at least one RBD in the up position (open; $O^{4}_{BA.2}$, $O^{5}_{BA.2}$, and $O^{6}_{BA.2}$) in a roughly 3:1 ratio of closed to open S (Figure 1B), which was higher than the $\sim$2:1 ratio we had observed for the BA.1 S (Gobeil et al., 2022). The 1-RBD-up populations, $O^{4}_{BA.2}$ and $O^{5}_{BA.2}$, differed primarily by the position of the up-RBD, while $O^{6}_{BA.2}$ had 1 RBD in the up position and a second RBD was partially up. Of the three BA.2 3-RBD-down S protein structures, $O^{2}_{BA.2}$ and $O^{3}_{BA.2}$ were more symmetric than the third, $O^{1}_{BA.2}$, which showed asymmetry in RBD dispositions between its three protomers, with $O^{2}_{BA.2}$ and $O^{3}_{BA.2}$ being more similar to each other than either was to the $O^{1}_{BA.2}$ structure (Data S3). Despite its heavily mutated RBD (Figure 1C), the Omicron BA.2 S ectodomain showed robust binding to an ACE2 receptor ectodomain construct, at levels similar to that of the BA.1 S ectodomain and higher than the D614G S, showing that the large number of RBD mutations and the increased propensity for the 3-RBD-down state do not impair the ability of the Omicron BA.2 S to bind ACE2 under the conditions of the ELISA assay (Figure 1D).

Thermostability of the SARS-CoV-2 Omicron BA.2 spike and RBD

We tested the thermostability of the D614G, BA.1, and BA.2 S protein ectodomains and of the corresponding monomeric RBD constructs using a differential scanning fluorimetry (DSF) assay that measures changes in protein intrinsic fluorescence as a function of temperature (Figures 2 and S1; Data S4). The wild-type (WT) RBD showed an inflection temperature (T_i) of $\sim$54.4°C (Figure 2B). The BA.1 RBD was substantially less stable with a T_i of $\sim$47.7°C. The reduced stability of the BA.1 RBD relative to the WT RBD is in close agreement with published reports (Lin et al., 2022). The thermostability of the BA.2 RBD, with a T_i of $\sim$50.4°C, was intermediate between that of the WT and BA.1 RBD. The D614G, BA.1, and BA.2 S proteins showed characteristic DSF profiles (Edwards et al., 2021). We have previously shown that the DSF profiles of SARS-CoV-2 S ectodomain, particularly the first inflection temperature (T_i#1), are sensitive to S stability. We observed a substantial decrease of T_i#1 for the BA.1 S ectodomain, but not for BA.2 S (Figures 2A and S1). Taken together, our results show stabilization of both the monomeric RBD (or RBD-only) construct and the S ectodomain in BA.2 relative to BA.1.

Intra- and interprotomer RBD packing in the 3-RBD-down Omicron BA.2 S protein

Cryo-EM maps of the 3-RBD-down (or closed) SARS-CoV-2 S protein have typically exhibited considerable disorder in the RBD densities, indicative of high mobility (Gobeil et al., 2021b). The most notably visible feature of the Omicron BA.2 S protein 3-RBD-down structures was their tightly packed and well-resolved RBDs (Figure 1B). We had observed close interprotomer RBD packing in the 3-RBD-down structures of the Omicron BA.1 S protein (Gobeil et al., 2022); this appeared further reinforced in the BA.2 S with the RBDs packed closer together (Figures 1B, 1C, 3, S2, and S4). In the BA.1 S, RBD-RBD contacts were mediated by a triad of acquired amino acid substitutions S371L/S373P/S375F that occurred within an interfacial RBD loop, with the S373P substitution restructuring the loop (relative to its structure in the D614G S), facilitating close interaction with another RBD interfacial loop harboring the Y505H substitution in the adjacent protomer (Figures 3D–3F and S4; Gobeil et al., 2022). The S373P, S375F, and Y505H substitutions observed at the RBD-RBD interface in the 3-RBD-down BA.1 S protein are also present in BA.2 (Figures 1A, 3A–3C, and S4). BA.2 has a S371F substitution instead of S371L in BA.1 (Figures 1A, 3B, and S4) and an additional T376A

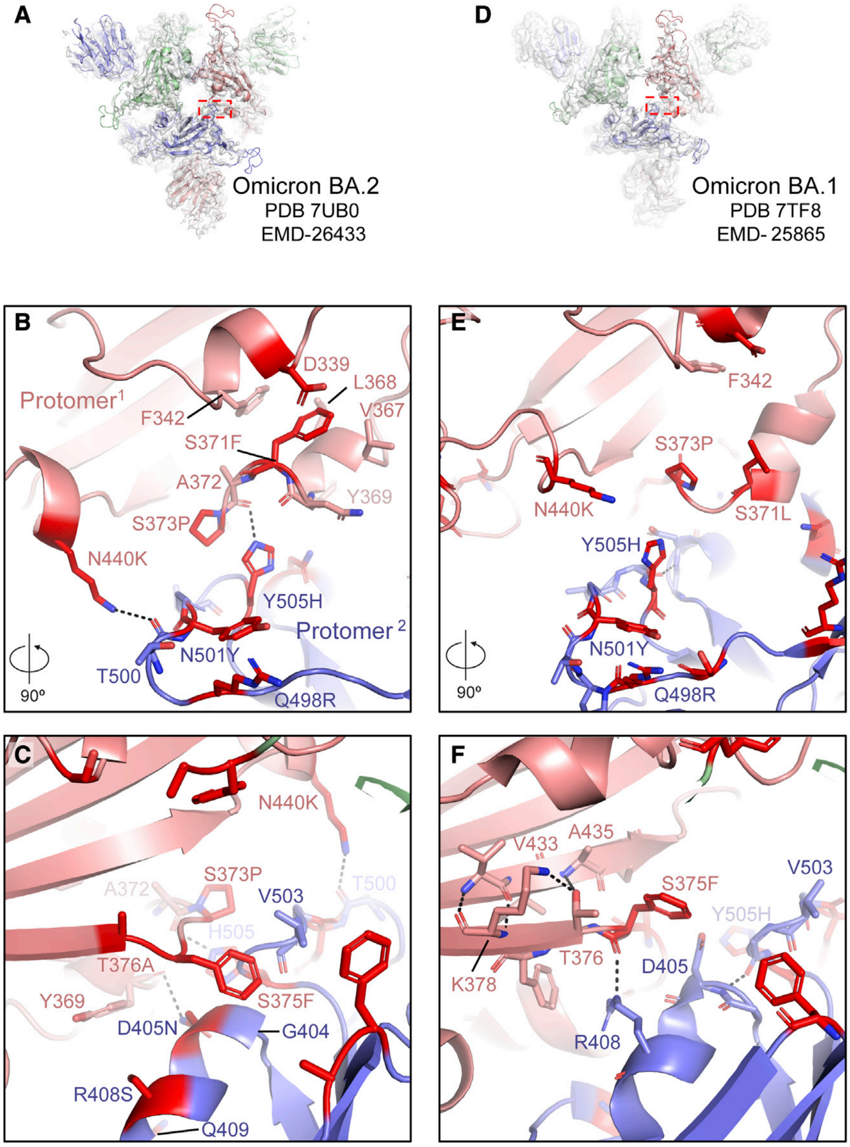

Figure 3. Omicron BA.2 S mutations induce RBD interfacial loop remodeling, facilitating tight packing of the 3-RBD-down state

(A) View of the Omicron BA.2 S protein $O^{1}_{BA.2}$ state with the red dotted rectangle indicating the region shown in (B) and (C).

(B and C) 90° rotated views of the interface between two RBDs in the 3-RBD-down $O^{1}_{BA.2}$ structure. The sites of mutation are colored red and the residues shown in sticks.

(D) Same as (A) but for the Omicron BA.1 S protein O1 state ($O^{1}_{BA.1}$), with the red rectangle indicating the region shown in (E) and (F).

(E and F) Same as (B) and (C) but for the Omicron BA.1 S protein $O^{1}_{BA.1}$ structure.

See also Figures S5, S7, S8, and S10.

substitution in this interfacial RBD loop (Figures 1A, 3C, 3F, and S4). The BA.2 S371F substitution results in van der Waals interaction of the bulkier F371 side chain with F342, resulting in closer packing of the two helical stretches 339–342 and 367–371 within the RBD (Figure 3B). The intraprotomer packing of these two helical stretches leading to a more compact RBD fold may be responsible for the increased thermostability observed for the BA.2 RBD relative to the BA.1 RBD (Figure 2B).

Due to the packing of the F371 side chain against the 367–371 helical turn within the BA.2 RBD, the region between residues 371 and 373 flips its position, bringing residue P373 closer to the RBD of the adjacent protomer, allowing its H505 side chain to stack against P373 (Figure 3B). In addition, due to the closer proximity of these two adjacent RBD interfacial loops, the H505 side chain can form an interprotomer hydrogen bond with the main chain carbonyl of residue A372. The loop bearing the Y505H substitution also incorporates two additional VOC mutations, N501Y and Q498R, that occur in both BA.1 and BA.2. Y501 and R498 engage in an intra-loop cation-π interaction conferring a defined structure to this region that remains invariant between BA.1 and BA.2 (Figures 3B and 3E). Although the internal structure of this cation-π stabilized loop remains invariant, as a consequence of the closer interprotomer interaction in BA.2 involving residue H505, this entire region spanning residues 494–507 is pulled closer to the adjacent protomer. Resulting from the close interprotomer packing of the two interfacial RBD loops, the side chain of K440 (from the N440K substitution that occurs in both BA.1 and BA.2) is positioned to engage in a hydrogen bond with the main chain of residue T500 from the adjacent protomer RBD (Figures 3B and S4).

Another structural change in this key 371–376 interfacial loop is orchestrated by the T376A substitution in the BA.2 RBD (Figures 3C and S4). In the BA.1 RBD, residue T376 is part of a β strand and its side chain engages in hydrogen bond interactions with the main chain of A435 in the adjacent β strand (Figure 3F). The loss of the side chain hydroxyl due to the T376A substitution in BA.2 disrupts this hydrogen bond, allowing A376 to move away from the β sheet, and as it does so, it pulls along the region around the S375F substitution so that F375 can now reach over to stack against the G404-Q409 helix and the V503 side chain of the adjacent protomer (Figures 3C and S4). Together with the restructuring of the 371–376 loop, concerted changes also occur in the adjacent protomer RBD that are key for forming the new interactions. The BA.2 S R408S substitution results in the disruption of an interprotomer hydrogen bond that the residue R408 side chain makes with the main chain carbonyl of residue 375 (Figures 3C, 3F, and S4). This releases F375 and facilitates its movement toward the adjacent RBD. The loss of the interprotomer H-bond due to the R408S substitution may be compensated

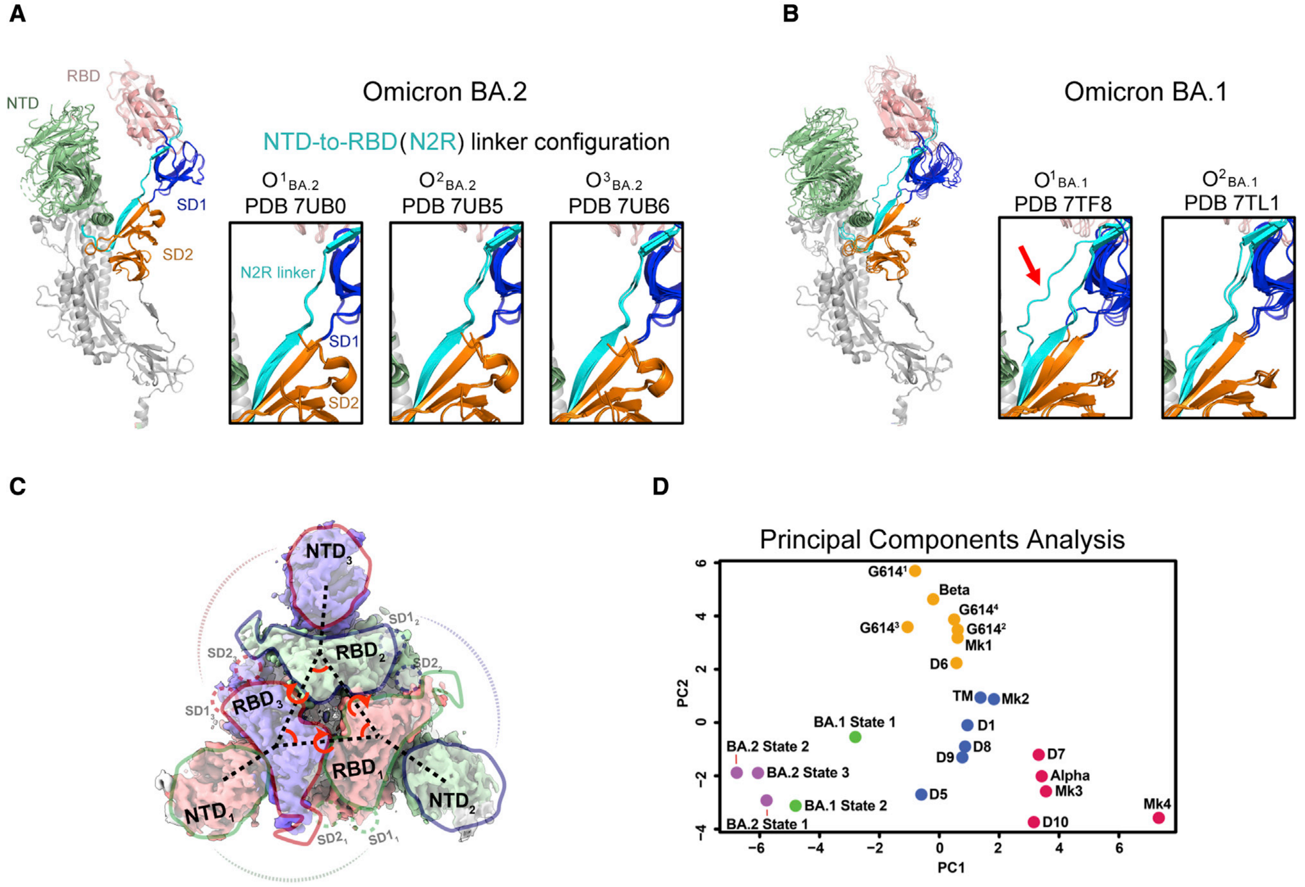

Figure 4. Intra- and interprotomer communication in the Omicron BA.2 3-RBD-down states

(A) Omicron BA.2 3-RBD-down structures shown with the three protomers aligned using S2 subunit residues 908–1,035. The structures are colored by domain; green, NTD; salmon, RBD; cyan, N2R linker; blue, SD1 subdomain; orange, SD2 subdomain; white, S2 subunit. The insets show zoomed-in views of the N2R region that connects the NTD and RBD within a protomer for the Omicron BA.2 S 3-RBD-down structures $O^1_{BA.2}$ (PDB: 7UB0), $O^2_{BA.2}$ (PDB: 7UB5), and $O^3_{BA.2}$ (PDB: 7UB6).

(B) Same as (A) but for the Omicron BA.1 3-RBD-down structures $O^1_{BA.1}$ (PDB: 7TF8) and $O^2_{BA.1}$ (PDB: 7TL1). The red arrow in (B) is pointing to the N2R rearranged state that was observed in one of the protomers in the $O^1_{BA.1}$ (PDB: 7TF8) structure.

(C) Interprotomer vectors describing the relationship between the NTDs, RBDs, and subdomains across protomers overlaid on the $O^1_{BA.2}$ (EMDB: 26433) cryo-EM reconstruction.

(D) Principal-component analysis of the interprotomer vector network distances, angle, and dihedrals for SARS-CoV-2 variant structures. Green, yellow, blue, and red points are K means cluster assignments (K = 4) for PCA of the dataset excluding the BA.2 variant. Each point represents a variant structure. The BA.2 structures are indicated by purple points. The variants shown include D614G (G614^1, G614^2, G614^3, and G614^4), Alpha, Beta, Delta (D1, D5, D6, D7, D8, D9, and D10); a spike (TM) with substitutions in three RBD position—K417, E484, and N501—that are mutated in multiple variants, including Gamma and Beta; a mink-associated variant (Mk1, Mk2, Mk3, and Mk4); BA.1 state 1 ($O^1_{BA.1}$) and state 2 ($O^2_{BA.1}$); and BA.2 ($O^1_{BA.2}$, $O^2_{BA.2}$, and $O^3_{BA.2}$).

See also Figure S6.

by the BA.2 S D405N substitution that mediates an interprotomer H-bond with the main chain carbonyl of Y369 (Figure 3C).

Taken together, our results provide evidence for enhanced interprotomer RBD-RBD packing in the 3-RBD-down BA.2 S relative to the BA.1 S, orchestrated by residue substitutions that remodel interfacial RBD loops to engineer their close packing within each RBD, as well as between RBDs in the closed S.

Intra- and interprotomer communication in the Omicron BA.2 3-RBD-down spike

We previously recognized a stretch of residues that connect the NTD and RBD within a protomer to be a modulator of RBD up and down transitions (Figure 4; Gobeil et al., 2021a, 2022). In an RBD-down protomer, this NTD-to-RBD ("N2R") linker interacts with the SD1 and SD2 subunits by contributing a β strand to each subdomain. An Omicron BA.1 S protein 3-RBD-down structure (named $O^1_{BA.1}$; PDB: 7TF8) stabilized a rearrangement in the N2R linker, possibly predisposing this protomer to adopt the RBD-up configuration (Figure 4B; Gobeil et al., 2022). We had also found this N2R rearranged state in other variants, albeit to lesser extents, suggesting that this N2R rearranged state may be an intermediate in the RBD up and down transition. In the Omicron BA.1 S cryo-EM dataset, we had also identified another 3-RBD-down population (named $O^2_{BA.1}$; PDB: 7TL1) that did

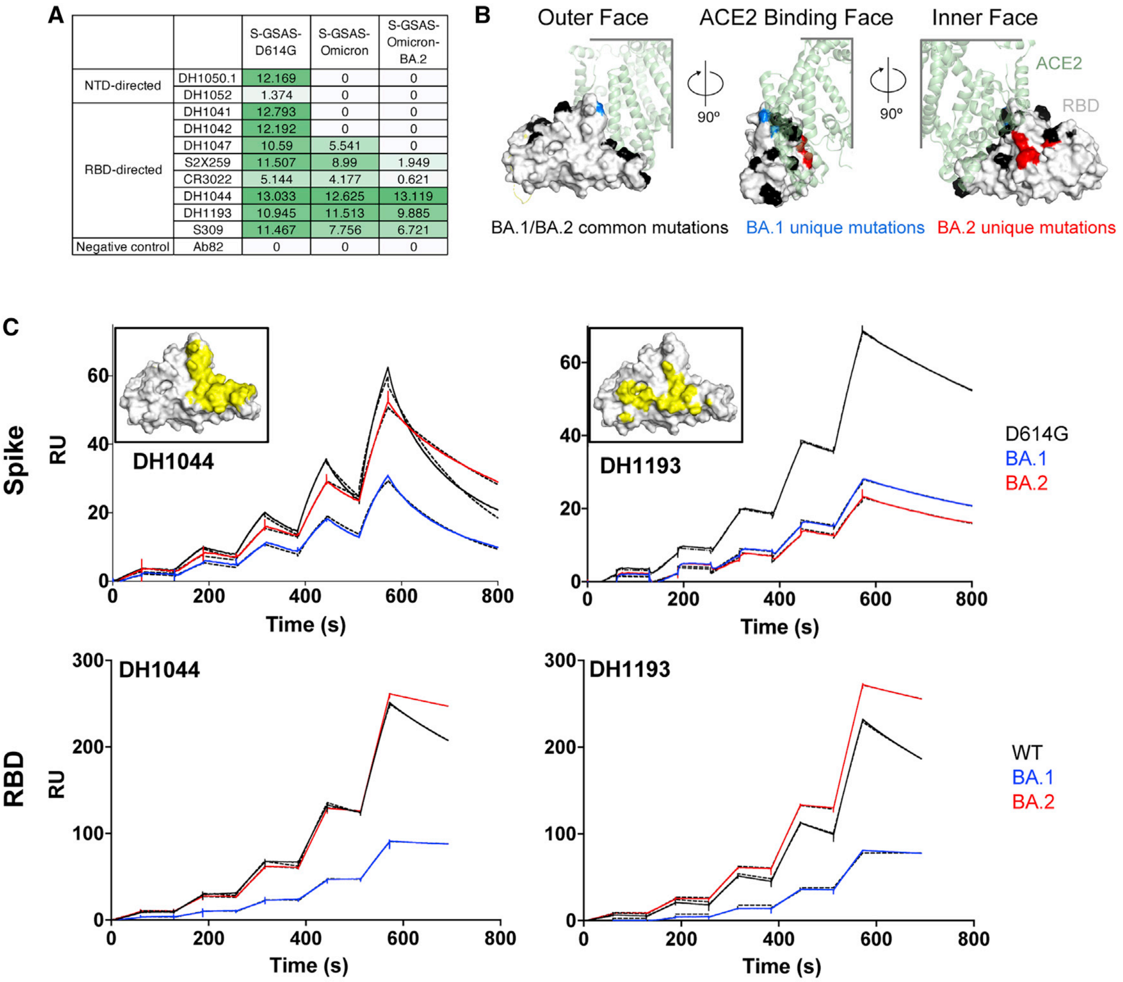

		S-GSAS-D614G	S-GSAS-Omicron	S-GSAS-Omicron-BA.2
NTD-directed	DH1050.1	12.169	0	0
	DH1052	1.374	0	0
RBD-directed	DH1041	12.793	0	0
	DH1042	12.192	0	0
	DH1047	10.59	5.541	0
	S2X259	11.507	8.99	1.949
	CR3022	5.144	4.177	0.621
	DH1044	13.033	12.625	13.119
	DH1193	10.945	11.513	9.885
	S309	11.467	7.756	6.721
Negative control	Ab82	0	0	0

	S-GSAS-D614G			S-GSAS-Omicron BA.1			S-GSAS-Omicron BA.2		
	ka ($M^{-1}s^{-1}$)	kd (s^{-1})	Kd (nM)	ka ($M^{-1}s^{-1}$)	kd (s^{-1})	Kd (nM)	ka ($M^{-1}s^{-1}$)	kd (s^{-1})	Kd (nM)
DH1044	1.3E6	4.9E-3	3.7	3.4E6	7.2E-3	2.1	8.9E5	2.5E-3	2.9
DH1193	7.5E5	1.2E-3	1.6	1.1E6	1.3E-3	1.2	1.4E5	1.6E-3	1.2

	WT RBD			Omicron BA.1 RBD			Omicron BA.2 RBD		
	ka ($M^{-1}s^{-1}$)	kd (s^{-1})	Kd (nM)	ka ($M^{-1}s^{-1}$)	kd (s^{-1})	Kd (nM)	ka ($M^{-1}s^{-1}$)	kd (s^{-1})	Kd (nM)
DH1044	1.8E6	2.7E-3	1.5	4.1E5	2.7E-4	0.65	4.5E5	1.0E-3	2.3
DH1193	3.3E5	3.0E-2	92.5	1.7E5	1.7E-6	0.01	3.9E6	9.0E-2	2.3

Figure 5. Antigenicity of the SARS-CoV-2 Omicron BA.2 S protein

(A) Antibody binding to SARS-CoV-2 S proteins measured by ELISA. The binding values were obtained by calculating area under curve of ELISA binding curves shown in Figure S11 and are color coded with a dark green to white gradient where dark green indicates tighter binding and white indicates no binding.

(B) Locations of Omicron BA.1 and BA.2 mutations mapped on the RBD surface. The RBD surface is shown in light gray, with the mutations that are common between BA.1 and BA.2 colored black; those that occur only in BA.1, but not in BA.2, are colored blue; and those that occur in BA.2, but not in BA.1, are colored red. ACE2 is shown bound to the RBD in transparent green cartoon representation.

(legend continued on next page)

not show this N2R rearrangement (Figure 4B; Gobeil et al., 2022). Examining the N2R region in the Omicron BA.2 S 3-RBD-down structures, we found that none of them showed the N2R rearrangement that we had observed in the Omicron BA.1 $O^1_{BA.1}$ structure (Figures 4A and 4B), with the three protomers within each structure aligning well in the N2R region (Figure 4A).

We previously defined a set of vectors that report on the overall domain organization of the S protein (Figure 4C; Gobeil et al., 2021b, 2022; Henderson et al., 2020). Analyzing the BA.2 S 3-RBD-down structures using principal-component analysis (PCA) of our previously described interprotomer vectors, we showed that the Omicron BA.2 S 3-RBD-down structures clustered close to the BA.1 S 3-RBD-down structures and were separated from the other variants included in this analysis (Figure 4D). The three BA.2 3-RBD-down S structures cluster closely together in a region of the PCA space closest to the $O^2_{BA.1}$ structure. This is consistent with the observed RBD-RBD packing in both the BA.1 and BA.2 S ectodomain structures.

Taken together, our structural studies show that the acquired Omicron BA.2 S mutations lead to further stabilization of the 3-RBD-down state compared with the BA.1 S protein and, through restructuring of the RBD-RBD interface, result in additional stabilizing interprotomer interactions.

Antigenicity of the Omicron BA.2 S protein

To assess the antigenic impact of the Omicron BA.2 S mutations, we tested binding of S-directed antibodies to two different S protein fragments: a monomeric RBD-only construct and the S protein ectodomain (S-GSAS platform) that were used in our cryo-EM structural analysis, here and in previously published studies (Gobeil et al., 2021a, 2021b, 2022; Figure 5; Data S5). We tested binding of two representative NTD-directed antibodies: the neutralizing antibody DH1050.1 that targets an antigenic supersite in the NTD and antibody DH1052 that recognizes a different NTD epitope and is non-neutralizing in *in vitro* assays but protects against SARS-CoV-2 challenge in animal models (Data S6; McCallum et al., 2021; Li et al., 2021). Both NTD-directed antibodies lost binding to the BA.1 and BA.2 S ectodomains. For testing RBD-directed antibodies, we chose representative examples of receptor-binding motif (RBM)-targeting antibodies (DH1041 and DH1042), RBD inner-face-targeting antibodies (DH1047, S2X259, and CR3022), and RBD outer-face-targeting antibodies (DH1044, DH1193, and S309) (Figure 5A; Li et al., 2021; Gobeil et al., 2022; Tortorici et al., 2021; Pinto et al., 2020). The RBM-targeting antibodies DH1041 and DH1042 bound the D614G S but lost binding to both Omicron BA.1 and BA.2 Ss, consistent with the accumulation of escape mutations around the ACE2 binding ridge (Figure 5B).

Of the RBD outer-face-binding antibodies tested, S309 lost ~40% binding to the BA.2 S relative to the D614G construct, consistent with the loss of its neutralization efficacy against BA.2 (Iketani et al., 2022; Takashita et al., 2022), although a recent study has reported that, although S309 has lost neutralization activity, it still retains protective efficacy against three SARS-CoV-2 Omicron sub-lineages (BA.1, BA.1.1, and BA.2) (Case et al., 2022). We had previously reported two antibodies, DH1044 and DH1193, that bind the outer RBD face and retain neutralizing activity against Omicron BA.1 (Li et al., 2021; Gobeil et al., 2022). Both antibodies retained nM binding affinity to the BA.2 RBD-only and S protein ectodomain constructs (Figure 5C) and effectively neutralized Omicron BA.1, BA.2, and BA.3 in a pseudovirus neutralization assay (Figure S5). We observed tight, low nM binding of DH1044 Fab to the D614G, BA.1, and BA.2 S proteins and the corresponding RBD constructs (Figure 5C). DH1044 binding profiles to S constructs followed the same trend as its binding to the RBD-only constructs, with the D614G/WT and BA.2 S/RBD binding at similar levels, while the BA.1 constructs showed lower level of binding. In contrast, DH1193 bound the BA.2 RBD-only construct at higher levels than it did the WT RBD construct, while the BA.2 S ectodomain bound DH1193 at a substantially lower level relative to the D614G S (Figure 5C). This difference in binding levels despite similar affinities is likely due to conformational effects that occur in the context of the S protein and are not present in the RBD-only context. As DH1193 binds to an RBD up conformation (Gobeil et al., 2022), its binding level to the BA.2 S may be diminished due to the lower propensity of the BA.2 S to adopt the RBD up configuration, thus resulting in fewer available binding sites. DH1044, on the other hand, binds the RBD-down state; thus, its epitope is not similarly constrained by S conformational dynamics.

One of the most dramatic antigenic consequences of the Omicron BA.2 mutations is the elimination of class-4-antibody-neutralizing activity (Barnes et al., 2020; Iketani et al., 2022). Of note, antibody S2X259 retains activity against Omicron BA.1 but is unable to neutralize BA.2 (Iketani et al., 2022; Cameroni et al., 2021; Tortorici et al., 2021). Of all the BA.2 RBD point mutations tested, including S371F, T376A, D405N, and R408S, S371F led to the most dramatic loss in neutralization activity in a pseudovirus neutralization assay (Iketani et al., 2022). A model of S2X259 bound to the BA.2 RBD (Figure 6) showed that the restructuring of the 371–376 RBD loop in the BA.2 S protein would result in a clash with the bound antibody. This was reflected in the binding of S2X259 to the Omicron S proteins (Figure 5A), where substantial binding was retained with the BA.1 S protein, but not to BA.2 S. Similar binding trends were also observed with the other class 4 antibodies CR3022 and DH1047 (Figure 6; Li et al., 2021; Yuan et al., 2020; Martinez et al., 2021). Like S2X259, the epitopes of DH1047 and CR3022 are likely to be disrupted by the restructuring of the 371–376 RBD loop.

(C) First row: binding of DH1044 and DH1193 Fabs to D614G (black), BA.1 (blue), and BA.2 (red) S protein ectodomains measured by SPR. Second row: binding of antibodies DH1044 and DH1193 to WT (black), Omicron-BA.1 (blue), and Omicron-BA.2 (red) RBD, measured by SPR using single-cycle kinetics, is shown. The solid lines are the binding sensorgrams; the dotted lines show fits of the data to a 1:1 Langmuir binding model. Affinity and kinetics of DH1044 and DH1193 Fab binding to the (top) S protein ectodomain and (bottom) monomeric RBD-only constructs are tabulated below. The insets show the binding footprints (colored yellow) of the DH1044 and DH1193 on the surface of the RBD (colored gray). The antibody binding footprints are obtained from previously published NSEM structures (Li et al., 2021; Gobeil et al., 2022). The RBD orientation shown in the inset figures is identical to that in the leftmost panel in (B).
See also Figures S11 and S12 and Table S1.

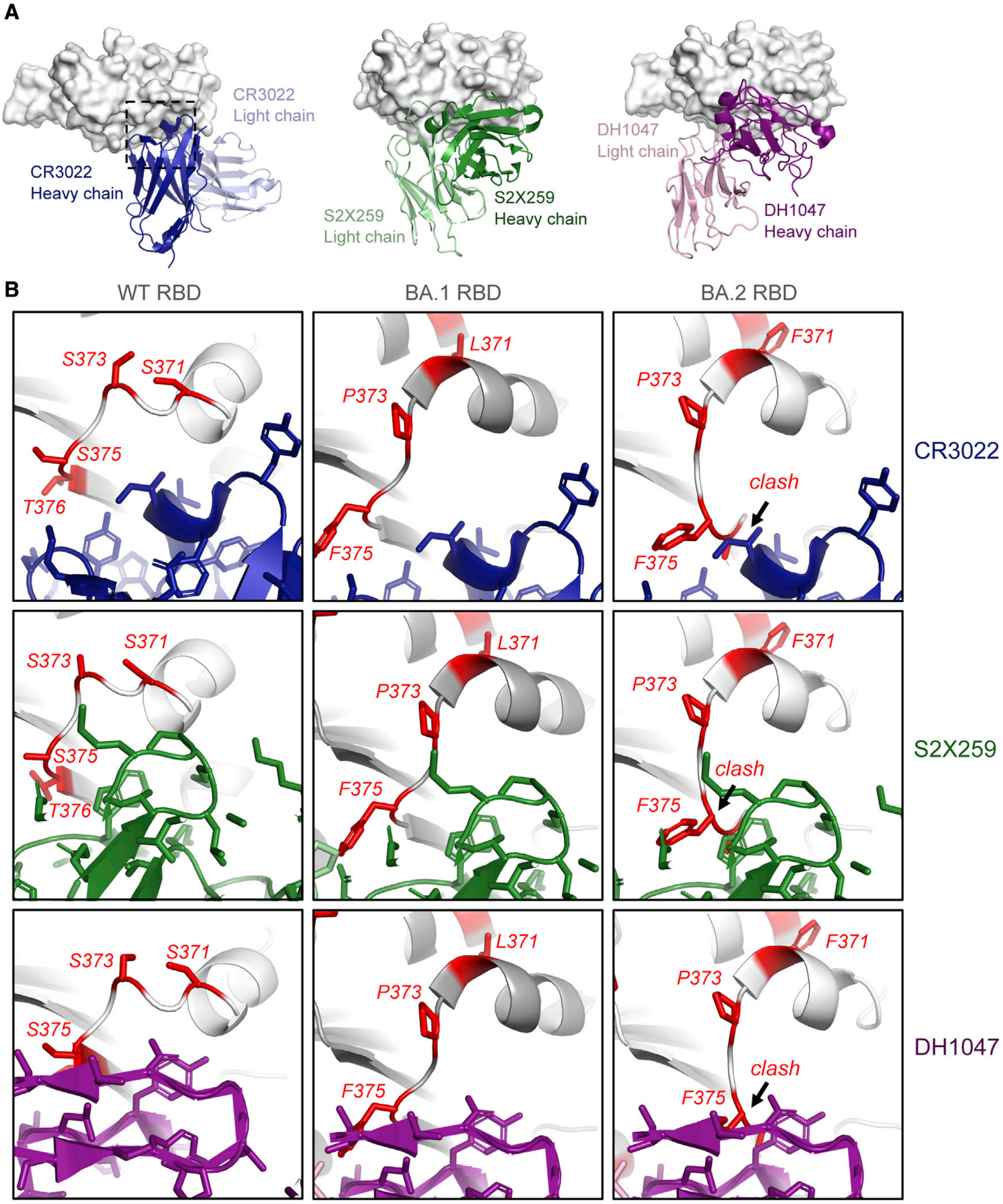

Figure 6. Structural basis for loss in binding of class 4 RBD-binding antibodies to Omicron BA.2 S protein

(A) (Left) Crystal structure of CR3022 bound to SARS-CoV-2 WT RBD (PDB: 7LOP), with the RBD shown as gray surface and CR3022 heavy and light chains colored dark blue and light blue, respectively. The dotted square indicates the zoomed-in areas shown in (B). (Middle) cryo-EM structure of S2X259 bound to SARS-CoV-2 WT RBD (PDB: 7RAL) is shown, with the RBD shown as gray surface, and S2X259 heavy and light chains colored dark green and light green, respectively. (Right) cryo-EM structure of DH1047 bound to SARS-CoV-2 WT RBD (PDB: 7LD1) is shown, with the RBD shown as gray surface, and DH1047 heavy and light chains colored dark magenta and light pink, respectively.

(B) Zoomed-in images of antibodies CR3022 (blue; PDB: 7LOP), S2X259 (green; PDB: 7RAL), and DH1047 (magenta; PDB: 7LD1), bound to WT RBD (leftmost panels). The middle and right panels show models of the antibodies bound to BA.1 (PDB: 7TF8) and BA.2 (PDB: 7UBO) RBDs. The models were prepared by aligning the variant RBDs with the antibody-bound RBD in each structure. For the WT RBD, residues that are mutated in the Omicron BA.2 variant are colored red and shown as sticks. For the BA.1 and BA.2 RBDs, the mutated residues in each are colored red. A region where the RBD 371–376 loop clashes with the antibody is indicated in the BA.2 RBD-bound models.

See also Figures S11 and S12.

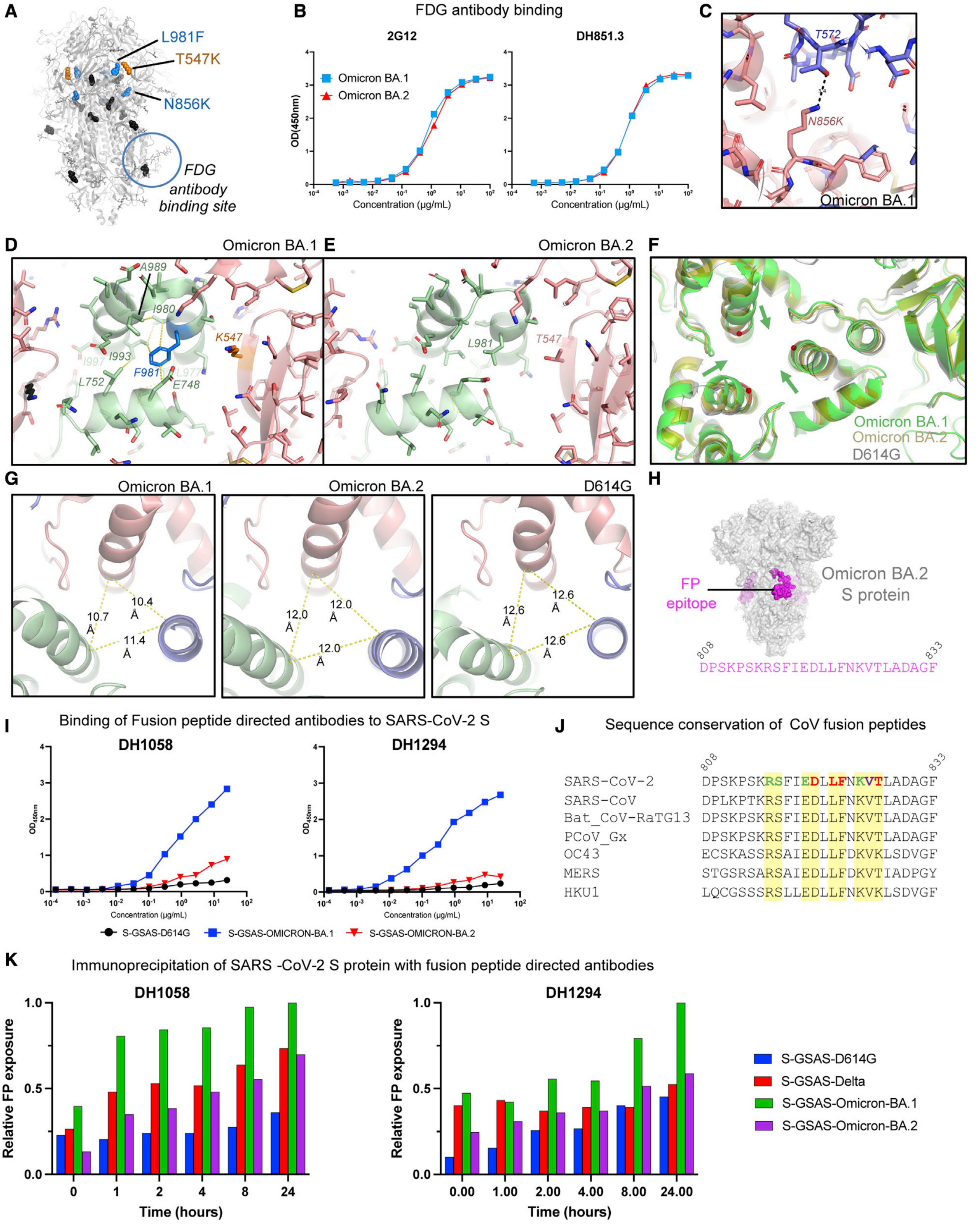

(legend on next page)

In summary, these results show that the acquired mutations in the Omicron BA.2 S protein affect the binding of RBD-directed antibodies by conformational effects related to the RBD up and down transitions in the context of the S as well as by conformational changes within the RBD itself.

Conformational changes in the S2 subunit of the Omicron BA.2 S protein

Omicron BA.1 and BA.2 S proteins share all but two S2 subunit mutations; the N865K and L981F substitutions in BA.1 do not occur in the BA.2 S (Figures 1A and 7A). Within the S2 subunit is a quaternary glycan cluster that binds to Fab-dimerized, glycan-reactive (FDG) antibodies (Williams et al., 2021). We found similar levels of binding of FDG antibodies 2G12 and DH851.3 to the Omicron BA.1 and BA.2 S proteins (Figure 6B). Given the previously observed sensitivity of FDG antibody binding to S2 subunit conformational changes (Edwards et al., 2021; Gobeil et al., 2022), this suggested that the differences at S2 residue positions 856 and 981 do not cause substantial changes to the overall conformation of the pre-fusion BA.2 S S2 subunit.

We next examined the local regions around the mutations that were different between BA.1 and BA.2. The N856K substitution in BA.1 introduced an interprotomer hydrogen bond involving the side chains of K856 and T572 (Figure 7C). The absence of this mutation in BA.2 could lead to local destabilization in this region relative to BA.1. The L981F mutation in the BA.1 S protein occurs in a structurally important region, proximal to residues K986 and V987 at the junction of the heptad repeat 1 (HR1) and central helix (CH), where engineering two consecutive prolines, the commonly used “2P” mutations, blocks the transition from pre- to post-fusion conformation (Wrapp et al., 2020; Pallesen et al., 2017). In the Omicron BA.1 structure, F981 inserts into a pocket between three interprotomer helices and in doing so sets up an extensive van der Waals interaction network involving residues E748, L752, L977, I980, A989, I993, and I997 (Figure 7D). Interestingly, the lone T547K SD1 subdomain mutation in BA.1 (not present in BA.2) is next to the helical segment that contains residue F981, with the K547 side chain stacked against this helix. The less bulky L981 in the Omicron BA.2 S cannot mediate the van der Waals network that F981 does in the BA.1 S protein (Figure 7E). We asked whether there were any changes in the local region around this mutation and found that the CH helices in the Omicron BA.1 S are pulled toward the central trimer axis relative to the positions of these helices in the D614G and BA.2 S proteins (Figure 7F). To quantify the extent of this shift, we measured the distances between Cα of residue 995 (Figure 7G) and found that the D614G S helices showed the greatest separation with the 995 Cαs 12.6 Å apart. The Omicron BA.2 helices are slightly closer together with a separation of 12 Å between the residue 995 Cα atoms, whereas the Omicron BA.1 helices were on average ~2 Å closer, with the distances showing more asymmetry with values of 10.4 Å, 10.7 Å, and 11.4 Å. As noted, these local changes did not percolate globally through the structure, as conformation-sensitive recognition of the glycan patch by FDG antibodies remained unchanged (Figures 7A and 7B).

We next probed the conformation of the FP region using FP-directed antibodies, DH1058 and DH1294 (Li et al., 2021; Gobeil et al., 2021b, 2022; Figures 7H–7K and S6; Data S7). Both antibodies mapped by ELISA to a 25-amino-acid peptide spanning the SARS-CoV-2 FP region (Figure 7H; Li et al., 2021; Gobeil et al., 2021b). Like DH1058, DH1294 bound diverse CoV S proteins (Figure S6; Data S7). Analysis of the FP sequences in these diverse S proteins revealed striking conservation of the residues that were identified as DH1058 antibody contacts in a crystal structure of DH1058 bound to the FP (PDB: 7TOW) (Figure 7J; Gobeil et al., 2022). We had previously observed increased accessibility of the Omicron BA.1 FP (relative to the FP in D614G and Delta variant S proteins) to DH1058 binding by ELISA (Gobeil et al., 2022). We observed similar enhanced binding of the Omicron BA.1 S to DH1294, while both DH1058 and DH1294 bound the Omicron BA.2 S at much lower levels (Figure 7I), suggesting that the BA.2 FP was less accessible to the FP-directed antibodies compared with the BA.1 FP. Immunoprecipitation assays showed time-dependent enhancement of binding upon incubation of the FP-directed antibodies with SARS-CoV-2 S ectodomain constructs, with Omicron BA.1 showing the highest levels of binding (Figure 7K; Data S7).

In summary, our structural analysis and binding data reveal differences in the S2 subunit between the Omicron BA.1 and BA.2 S

Figure 7. Conformation and antigenicity of the S2 subunit of the Omicron BA.2 S protein

(A) Omicron BA.1 S shown in gray with S2 and SD1 mutations shown as spheres. The S2 mutations that BA.1 and BA.2 have in common are colored black. The L981F and N856K substitutions that occur in the BA.1, but not in the BA.2, S are colored blue, and the SD1 T547K substitution that occurs in BA.1, but not in the BA.2, S is colored orange. The glycan cluster that binds Fab-dimerized glycan-reactive (FDG) antibodies is marked with a circle.

(B) Binding of FDG antibodies 2G12 and DH851.3 to Omicron BA.1 and BA.2 S proteins.

(C) Zoom in of the region around the N856K substitution in the BA.1 S, showing an interprotomer hydrogen bond between K856 and T572.

(D) Zoom in of the region around the L981F and T547K substitutions in the Omicron BA.1 spike. The yellow dotted lines indicate van der Waals contacts.

(E) Same as in (D) but for the Omicron BA.2 S.

(F) Overlay of the D614G, BA.1, and BA.2 Ss, showing the movement of the BA.1 S2 subunit helices toward the center of the trimer axis.

(G) View of the S2 subunit helices, showing interprotomer distances between the Cα atom of residue R995, which was used to measure the differences in the arrangement of this region between the different Ss.

(H) Omicron BA.2 spike with the location of the fusion peptide shown in magenta. The sequence below spans the magenta regions mapped on the structure.

(I) ELISA binding of antibodies (left) DH1058 and (right) DH1294 to the D614G (black), BA.1 (blue), and BA.2 (red) S protein ectodomains.

(J) Sequence alignment of the fusion peptide region in diverse CoV S proteins. In the SARS-CoV-2 sequence, the colored residues indicate contacts observed with FP-directed antibody DH1058 in the crystal structure of FP bound to DH1058 (PDB: 7TOW). Red indicates residues that make both main-chain and side-chain contacts, green indicates residues that only make side-chain contacts, and purple indicates residues that contact DH1058 only through the main chain. Contacts indicated here include both direct contact with the antibody as well as water-mediated contacts.

(K) Time-dependent exposure of fusion peptide (FP) to FP-directed antibodies, DH1058 and DH1294, shown as relative FP exposure ranging from 0 to 24 h.
See also Figures S14 and S15.

proteins, including differences in the configuration of the critical HR1-CH region and altered FP accessibility.

DISCUSSION

The emergence of the SARS-CoV-2 Omicron variant triggered widespread alarm due to its highly mutated S protein (Viana et al., 2022). The rapid spread of the Omicron variant was at first dominated by its BA.1 sub-lineage (Data S1). In time, a second Omicron sub-lineage, BA.2, started spreading and has now overtaken the BA.1 in several locations. As the S protein is central to several properties that influence the spread of a variant, here, we determined structures of the BA.2 S to compare them with our previously determined structures of the Omicron BA.1 S protein, aiming to arrive at a structure-guided understanding of the similarities and differences between the S-protein-driven properties of these two phylogenetically related sub-lineages.

A unifying structural feature of the Omicron variant is the tight packing of its RBDs in the 3-RBD-down (or closed) S where the receptor binding site and many immunodominant epitopes are inaccessible. We previously recognized that an interfacial RBD loop in the BA.1 S protein containing three mutations—S371L, S373P, and S375F—mediates interprotomer RBD-RBD packing in the closed Omicron BA.1 S protein (Gobeil et al., 2022). The BA.2 S protein incorporates additional strategically positioned mutations in this interfacial RBD loop, leading to restructuring of this region and facilitating both improved internal packing of the RBD core as well as improved packing of the RBD-RBD interface in the 3-RBD-down S. We expect the S proteins of the BA.3, BA.4, and BA.5 Omicron variant sub-lineages will also have similarly tightly packed 3-RBD-down states, as they all contain the key S371F, S373P, and S375F mutations of BA.2. In addition, the BA.4 and BA.5 S proteins also include the T376A substitution that occurs in the BA.2 S (but not in BA.1 and BA.3). The increased stabilization of the closed state may result in low immunogenicity of the S protein, which may translate to less effective protection from an Omicron infection for unvaccinated individuals without prior infection by any other variant. For the same reason, a vaccine based on the Omicron S may exhibit lowered immunogenicity, as large proportions of the immunogenic RBD sites would be occluded. This mutation-induced remodeling of intra- and inter-RBD structures contributes to the higher immune evasion observed in BA.2, particularly the loss in activity of class 4 RBD-directed antibodies (Barnes et al., 2020; Iketani et al., 2022), where we showed that a combination of local structural effects caused by the RBD mutations, as well as S conformational effects, may play a role in the dramatic loss in activity observed. The mutation-induced remodeling of the internal structure of the BA.2 RBD has implications for design of RBD and S-based immunogens, where the higher stability of the BA.2 RBD may result in more robust immunogens than its BA.1 counterpart.

Even though the BA.2 S showed better interprotomer RBD packing in the closed state than the BA.1 S, they both bound similar levels of ACE2 receptor in our *in vitro* ELISA assay, suggesting that the receptor binding competencies remain similar between the two variants despite their modified interprotomer associations. We observed differences between the BA.1 and BA.2 S proteins in the accessibility of the FP. Our results demonstrating that these FP-directed antibodies can induce FP exposure provide intriguing insights into the mechanism of action of these broadly reactive antibodies and the dynamics of this functionally critical and highly conserved S2 subunit region. While FP-directed antibodies like DH1058 and DH1294 are non-neutralizing, it remains to be determined whether they are protective *in vivo*. Being able to effectively target these highly conserved regions could lead to strategies to elicit broad protective responses to counteract future variants or CoV outbreaks.

The key differences in the BA.1 and BA.2 S proteins include (1) better reinforced RBD-RBD packing in the BA.2 closed state, (2) better internal packing of the BA.2 RBD, and (3) a less accessible FP. All these factors, as well as the absence of the N2R rearranged state observed in the BA.1 3-RBD-down $O^1_{BA.1}$ structure, suggest a more stable architecture of the BA.2 S compared with the BA.1 S. Over the course of SARS-CoV-2 evolution, particularly in variants that have emerged to become VOCs, we have observed the S proteins balance between stability of the pre-fusion state with features such as greater propensity to adopt a more open state that may lead to greater transmissibility (Gobeil et al., 2021b; Zhang et al., 2021, 2022; Zhou et al., 2022). In the BA.2 S, we see the balance tilt toward greater stability relative to BA.1. It is tempting to speculate that the structural features that make the S protein in BA.1 less stable than in BA.2, including increased propensity for the RBD to transition to the up state and more facile release of the FP, may have contributed to its rapid spread during the start of the Omicron wave, while the greater stability of the BA.2 S and its increased immune evasion properties may be allowing it to make its current gains in the wake of a receding BA.1 wave.

Overall, our studies uncover defining characteristics of the Omicron variant and, through atomic-level structural determination, assign purpose to key mutations. They further highlight striking differences in functional regions between the BA.1 and BA.2 sub-lineages that could be responsible for differences in their biology.

Limitations of the study

Despite higher proportion of 3-RBD-down S proteins observed in the BA.2 S ectodomain cryo-EM dataset, we observed similar levels of ACE2-binding BA.1 and BA.2 S proteins by ELISA. The ACE2 density in the ELISA format may not be representative of physiological ACE2 receptor density, and differences in ACE2 binding of the BA.1 and BA.2 S proteins may be observed in physiological conditions. In addition, one or more of the unique mutations between BA.1 and BA.2 S proteins may contribute to increased ACE2 binding of the BA.2 S that may offset, to some extent, the increased proportion of closed BA.2 S. Detailed mutagenesis and binding studies will be needed to accurately parse the effect of the BA.1 and BA.2 mutations on their ACE2-binding levels.

Our structures of the 3-RBD-down BA.2 S proteins reveal atomic-level details of mutation-induced remodeling of the RBD, leading to better intra- and interprotomer packing. Further mutational studies and careful evaluation of point mutants will be required to clarify the contribution of each substitution on the observed differences in the BA.2 S architecture.

STAR★METHODS

Detailed methods are provided in the online version of this paper and include the following:

- KEY RESOURCES TABLE
- RESOURCE AVAILABILITY
    - Lead contact
    - Materials availability
    - Data and code availability
- EXPERIMENTAL MODEL AND SUBJECT DETAILS
    - Cell culture
- METHOD DETAILS
    - Plasmids
    - Protein purification
    - Differential scanning fluorimetry
    - ELISA assays
    - Surface plasmon resonance
    - Sensogram data were analyzed using the BiaEvaluation software (Cytiva, MA)
    - Vector based structure analysis
    - Difference distance matrices (DDM)
    - Pseudovirus neutralization assay
    - Immunoprecipitation assays
- QUANTIFICATION AND STATISTICAL ANALYSIS

SUPPLEMENTAL INFORMATION

Supplemental information can be found online at https://doi.org/10.1016/j.celrep.2022.111009.

ACKNOWLEDGMENTS

cryo-EM data were collected at the Duke Krios at the Duke University Shared Materials Instrumentation Facility (SMIF), a member of the North Carolina Research Triangle Nanotechnology Network (RTNN), which is supported by the National Science Foundation (award number ECCS-2025064) as part of the National Nanotechnology Coordinated Infrastructure (NNCI). This study utilized the computational resources offered by Duke Research Computing (http://rc.duke.edu; NIH 1S10OD018164-01) at Duke University. This work was supported by NIH R01 AI145687 (P.A. and W.W.) and AI165147 (P.A. and R.C.H.) and NIH, NIAID, DMID grant P01 AI158571 (B.F.H.).

AUTHOR CONTRIBUTIONS

V.S. and P.A. determined cryo-EM structures and prepared the first draft of the manuscript. J.L. purified RBD and spike proteins and performed surface plasmon resonance (SPR) experiments. V.S., S.M.-C.G., R.H., A.M., and P.A. analyzed structures. S.M.-C.G. performed immunoprecipitation assays. R.P., M.B., M.D., and M.M. performed ELISA assays. K.J., X.H., A.M., M.S., and E.B. expressed and purified proteins. R.J.E. performed negative stain electron microscopy (NSEM) analysis. K.W. and W.W. analyzed data. K.O.S., B.K., and X.L. provided key reagents. B.F.H. provided S RBD and S2 antibodies, supervised ELISA assays, and edited the manuscript. All authors reviewed and approved the manuscript. P.A. supervised the study and reviewed all data.

DECLARATION OF INTERESTS

B.F.H., K.O.S., B.K., X.L., R.J.E., S.M.-C.G., and P.A. are named in patents submitted on the SARS-CoV-2 monoclonal antibodies studied in this paper. Other authors declare no competing interests.

Received: April 14, 2022
Revised: May 23, 2022
Accepted: June 3, 2022
Published: June 28, 2022

REFERENCES

Afonine, P.V., Poon, B.K., Read, R.J., Sobolev, O.V., Terwilliger, T.C., Urzhumtsev, A., and Adams, P.D. (2018). Real-space refinement inPHENIXfor cryo-EM and crystallography. Acta. Crystallogr. D Struct. Biol. *74*, 531–544. https://doi.org/10.1107/s2059798318006551.

Barnes, C.O., West, A.P., Jr., Huey-Tubman, K.E., Hoffmann, M.A.G., Sharaf, N.G., Hoffman, P.R., Koranda, N., Gristick, H.B., Gaebler, C., Muecksch, F., et al. (2020). Structures of human antibodies bound to SARS-CoV-2 spike reveal common epitopes and recurrent features of antibodies. Cell *182*, 828–842.e16. https://doi.org/10.1016/j.cell.2020.06.025.

Cameroni, E., Bowen, J.E., Rosen, L.E., Saliba, C., Zepeda, S.K., Culap, K., Pinto, D., Vanblargan, L.A., De Marco, A., Di Iulio, J., et al. (2021). Broadly neutralizing antibodies overcome SARS-CoV-2 Omicron antigenic shift. Nature *602*, 664–670. https://doi.org/10.1038/s41586-021-04386-2.

Case, J.B., Mackin, S., Errico, J., Chong, Z., Madden, E.A., Guarino, B., Schmid, M.A., Rosenthal, K., Ren, K., Jung, A., et al. (2022). Resilience of S309 and AZD7442 monoclonal antibody treatments against infection by SARS-CoV-2 Omicron lineage strains. Preprint at bioRxiv. https://doi.org/10.1101/2022.03.17.484787.

Cerutti, G., Guo, Y., Liu, L., Liu, L., Zhang, Z., Luo, Y., Huang, Y., Wang, H.H., Ho, D.D., Sheng, Z., and Shapiro, L. (2022). Cryo-EM structure of the SARS-CoV-2 Omicron spike. Cell Rep. *38*, 110428. https://doi.org/10.1016/j.celrep.2022.110428.

Croll, T.I. (2018). ISOLDE: a physically realistic environment for model building into low-resolution electron-density maps. Acta. Crystallogr. D Struct. Biol. *74*, 519–530. https://doi.org/10.1107/s2059798318002425.

Cui, Z., Liu, P., Wang, N., Wang, L., Fan, K., Zhu, Q., Wang, K., Chen, R., Feng, R., Jia, Z., et al. (2022). Structural and functional characterizations of infectivity and immune evasion of SARS-CoV-2 Omicron. Cell *185*, 860–871.e13. https://doi.org/10.1016/j.cell.2022.01.019.

Edwards, R.J., Mansouri, K., Stalls, V., Manne, K., Watts, B., Parks, R., Janowska, K., Gobeil, S.M.C., Kopp, M., Li, D., et al. (2021). Cold sensitivity of the SARS-CoV-2 spike ectodomain. Nat. Struct. Mol. Biol. *28*, 128–131. https://doi.org/10.1038/s41594-020-00547-5.

Emsley, P., Lohkamp, B., Scott, W.G., and Cowtan, K. (2010). Features and development ofCoot. Acta. Crystallogr. Sect. D Biol. Crystallogr. *66*, 486–501. https://doi.org/10.1107/s0907444910007493.

Gilbert, P.B., Montefiori, D.C., Mcdermott, A.B., Fong, Y., Benkeser, D., Deng, W., Zhou, H., Houchens, C.R., Martins, K., Jayashankar, L., et al. (2022). Immune correlates analysis of the mRNA-1273 COVID-19 vaccine efficacy clinical trial. Science *375*, 43–50.

Gobeil, S.M., Henderson, R., Stalls, V., Janowska, K., Huang, X., May, A., Speakman, M., Beaudoin, E., Manne, K., Li, D., et al. (2022). Structural diversity of the SARS-CoV-2 Omicron spike. Mol. Cell. Date available online: March 24. https://doi.org/10.1016/j.molcel.2022.03.028.

Gobeil, S.M.C., Janowska, K., Mcdowell, S., Mansouri, K., Parks, R., Manne, K., Stalls, V., Kopp, M.F., Henderson, R., Edwards, R.J., et al. (2021a). D614G mutation alters SARS-CoV-2 spike conformation and enhances protease cleavage at the S1/S2 junction. Cell. Rep. *34*, 108630. https://doi.org/10.1016/j.celrep.2020.108630.

Gobeil, S.M.C., Janowska, K., Mcdowell, S., Mansouri, K., Parks, R., Stalls, V., Kopp, M.F., Manne, K., Li, D., Wiehe, K., et al. (2021b). Effect of natural mutations of SARS-CoV-2 on spike structure, conformation, and antigenicity. Science *373*, eabi6226. https://doi.org/10.1126/science.abi6226.

Goddard, T.D., Huang, C.C., Meng, E.C., Pettersen, E.F., Couch, G.S., Morris, J.H., and Ferrin, T.E. (2018). UCSF ChimeraX: meeting modern challenges in visualization and analysis. Protein. Sci. *27*, 14–25. https://doi.org/10.1002/pro.3235.

Grant, B.J., Skjærven, L., and Yao, X.Q. (2020). The Bio3D packages for structural bioinformatics. Protein. Sci. *30*, 20–30. https://doi.org/10.1002/pro.3923.

Hadfield, J., Megill, C., Bell, S.M., Huddleston, J., Potter, B., Callender, C., Sagulenko, P., Bedford, T., and Neher, R.A. (2018). Nextstrain: real-time tracking of pathogen evolution. Bioinformatics *34*, 4121–4123. https://doi.org/10.1093/bioinformatics/bty407.

Henderson, R., Edwards, R.J., Mansouri, K., Janowska, K., Stalls, V., Gobeil, S.M.C., Kopp, M., Li, D., Parks, R., Hsu, A.L., et al. (2020). Controlling the SARS-CoV-2 spike glycoprotein conformation. Nat. Struct. Mol. Biol. *27*, 925–933. https://doi.org/10.1038/s41594-020-0479-4.

Humphrey, W., Dalke, A., and Schulten, K. (1996). VMD: Visual molecular dynamics. J. Mol. Graph. *14*, 33–38. https://doi.org/10.1016/0263-7855(96)00018-5.

Iketani, S., Liu, L., Guo, Y., Liu, L., Chan, J.F.W., Huang, Y., Wang, M., Luo, Y., Yu, J., Chu, H., et al. (2022). Antibody evasion properties of SARS-CoV-2 Omicron sublineages. Nature *604*, 553–556. https://doi.org/10.1038/s41586-022-04594-4.

Li, D., Edwards, R.J., Manne, K., Martinez, D.R., Schäfer, A., Alam, S.M., Wiehe, K., Lu, X., Parks, R., Sutherland, L.L., et al. (2021). In vitro and in vivo functions of SARS-CoV-2 infection-enhancing and neutralizing antibodies. Cell *184*, 4203–4219.e32. https://doi.org/10.1016/j.cell.2021.06.021.

Liebschner, D., Afonine, P.V., Baker, M.L., Bunkóczi, G., Chen, V.B., Croll, T.I., Hintze, B., Hung, L.-W., Jain, S., Mccoy, A.J., et al. (2019). Macromolecular structure determination using X-rays, neutrons and electrons: recent developments in Phenix. Acta. Crystallogr. Sect. D Struct. Biol. *75*, 861–877. https://doi.org/10.1107/s2059798319011471.

Lin, S., Chen, Z., Zhang, X., Wen, A., Yuan, X., Yu, C., Yang, J., He, B., Cao, Y., and Lu, G. (2022). Characterization of SARS-CoV-2 Omicron spike RBD reveals significantly decreased stability, severe evasion of neutralizing-antibody recognition but unaffected engagement by decoy ACE2 modified for enhanced RBD binding. Signal. Transduct. Target. Ther. *7*, 56. https://doi.org/10.1038/s41392-022-00914-2.

Mannar, D., Saville, J.W., Zhu, X., Srivastava, S.S., Berezuk, A.M., Tuttle, K.S., Marquez, A.C., Sekirov, I., and Subramaniam, S. (2022). SARS-CoV-2 Omicron variant: antibody evasion and cryo-EM structure of spike protein-ACE2 complex. Science *375*, eabn7760–764. https://doi.org/10.1126/science.abn7760.

Martinez, D.R., Schäfer, A., Gobeil, S., Li, D., De La Cruz, G., Parks, R., Lu, X., Barr, M., Stalls, V., Janowska, K., et al. (2021). A broadly cross-reactive antibody neutralizes and protects against sarbecovirus challenge in mice. Sci. Transl. Med. *14*, eabj7125. https://doi.org/10.1126/scitranslmed.abj7125.

Mccallum, M., Czudnochowski, N., Rosen, L.E., Zepeda, S.K., Bowen, J.E., Walls, A.C., Hauser, K., Joshi, A., Stewart, C., Dillen, J.R., et al. (2022). Structural basis of SARS-CoV-2 Omicron immune evasion and receptor engagement. Science *375*, 864–868. https://doi.org/10.1126/science.abn8652.

Mccallum, M., De Marco, A., Lempp, F.A., Tortorici, M.A., Pinto, D., Walls, A.C., Beltramello, M., Chen, A., Liu, Z., Zatta, F., et al. (2021). N-terminal domain antigenic mapping reveals a site of vulnerability for SARS-CoV-2. Cell *184*, 2332–2347.e16. https://doi.org/10.1016/j.cell.2021.03.028.

Meng, B., Kemp, S.A., Papa, G., Datir, R., Ferreira, I.A.T.M., Marelli, S., Harvey, W.T., Lytras, S., Mohamed, A., Gallo, G., et al. (2021). Recurrent emergence of SARS-CoV-2 spike deletion H69/V70 and its role in the Alpha variant B.1.1.7. Cell Rep. *35*, 109292. https://doi.org/10.1016/j.celrep.2021.109292.

Pallesen, J., Wang, N., Corbett, K.S., Wrapp, D., Kirchdoerfer, R.N., Turner, H.L., Cottrell, C.A., Becker, M.M., Wang, L., Shi, W., et al. (2017). Immunogenicity and structures of a rationally designed prefusion MERS-CoV spike antigen. Proc. Natl. Acad. Sci. USA *114*, E7348–E7357. https://doi.org/10.1073/pnas.1707304114.

Pettersen, E.F., Goddard, T.D., Huang, C.C., Couch, G.S., Greenblatt, D.M., Meng, E.C., and Ferrin, T.E. (2004). UCSF Chimera?A visualization system for exploratory research and analysis. J. Comput. Chem. *25*, 1605–1612. https://doi.org/10.1002/jcc.20084.

Pinto, D., Park, Y.J., Beltramello, M., Walls, A.C., Tortorici, M.A., Bianchi, S., Jaconi, S., Culap, K., Zatta, F., De Marco, A., et al. (2020). Cross-neutralization of SARS-CoV-2 by a human monoclonal SARS-CoV antibody. Nature *583*, 290–295. https://doi.org/10.1038/s41586-020-2349-y.

Punjani, A., Rubinstein, J.L., Fleet, D.J., and Brubaker, M.A. (2017). cryoSPARC: algorithms for rapid unsupervised cryo-EM structure determination. Nat. Methods *14*, 290–296. https://doi.org/10.1038/nmeth.4169.

Sagulenko, P., Puller, V., and Neher, R.A. (2018). TreeTime: maximum-likelihood phylodynamic analysis. Virus Evol *4*, vex042. https://doi.org/10.1093/ve/vex042.

Scheres, S.H. (2012). RELION: implementation of a Bayesian approach to cryo-EM structure determination. J Struct Biol *180*, 519–530.

Scheres, S.H. (2016). Processing of Structurally Heterogeneous Cryo-EM Data in RELION. Methods Enzymol *579*, 125–157.

Schrodinger, L. (2015). The PyMOL Molecular Graphics System.

Shen, L., Trichee, T.J., Bard, J.D., Biegel, J.A., Judkins, A.R., and Gai, X. (2021). Spike Protein NTD mutation G142D in SARS-CoV-2 Delta VOC lineages is associated with frequent back mutations, increased viral loads, and immune evasion. Preprint at medRxiv. https://doi.org/10.1101/2021.09.12.21263475.

Takashita, E., Kinoshita, N., Yamayoshi, S., Sakai-Tagawa, Y., Fujisaki, S., Ito, M., Iwatsuki-Horimoto, K., Halfmann, P., Watanabe, S., Maeda, K., et al. (2022). Efficacy of antiviral agents against the SARS-CoV-2 omicron subvariant BA.2. N. Engl. J. Med. *386*, 1475–1477. https://doi.org/10.1056/nejmc2201933.

Team, R.C. (2017). R: A Language and Environment for Statistical Computing.

Tortorici, M.A., Czudnochowski, N., Starr, T.N., Marzi, R., Walls, A.C., Zatta, F., Bowen, J.E., Jaconi, S., Di Iulio, J., Wang, Z., et al. (2021). Broad sarbecovirus neutralization by a human monoclonal antibody. Nature *597*, 103–108. https://doi.org/10.1038/s41586-021-03817-4.

Viana, R., Moyo, S., Amoako, D.G., Tegally, H., Scheepers, C., Althaus, C.L., Anyaneji, U.J., Bester, P.A., Boni, M.F., Chand, M., et al. (2022). Rapid epidemic expansion of the SARS-CoV-2 Omicron variant in southern Africa. Nature *603*, 679–686. https://doi.org/10.1038/s41586-022-04411-y.

Williams, W.B., Meyerhoff, R.R., Edwards, R.J., Li, H., Manne, K., Nicely, N.I., et al. (2021). Fab-dimerized glycan-reactive antibodies are a structural category of natural antibodies. Cell *184*, 2955–2972.e25.

Wrapp, D., Wang, N., Corbett, K.S., Goldsmith, J.A., Hsieh, C.L., Abiona, O., Graham, B.S., and Mclellan, J.S. (2020). Cryo-EM structure of the 2019-nCoV spike in the prefusion conformation. Science *367*, 1260–1263. https://doi.org/10.1126/science.abb2507.

Ye, G., Liu, B., and Li, F. (2022). Cryo-EM structure of a SARS-CoV-2 omicron spike protein ectodomain. Nat. Commun. *13*, 1214. https://doi.org/10.1038/s41467-022-28882-9.

Yuan, M., Wu, N.C., Zhu, X., Lee, C.C.D., So, R.T.Y., Lv, H., Mok, C.K.P., and Wilson, I.A. (2020). A highly conserved cryptic epitope in the receptor binding domains of SARS-CoV-2 and SARS-CoV. Science *368*, 630–633. https://doi.org/10.1126/science.abb7269.

Zhang, J., Cai, Y., Lavine, C.L., Peng, H., Zhu, H., Anand, K., Tong, P., Gautam, A., Mayer, M.L., Rits-Volloch, S., et al. (2022). Structural and functional impact by SARS-CoV-2 Omicron spike mutations. Cell Rep. *39*, 110729. https://doi.org/10.1016/j.celrep.2022.110729.

Zhang, J., Cai, Y., Xiao, T., Lu, J., Peng, H., Sterling, S.M., Walsh, R.M., Jr., Rits-Volloch, S., Zhu, H., Woosley, A.N., et al. (2021). Structural impact on SARS-CoV-2 spike protein by D614G substitution. Science *372*, 525–530. https://doi.org/10.1126/science.abf2303.

Zhou, T., Wang, L., Misasi, J., Pegu, A., Zhang, Y., Harris, D.R., Olia, A.S., Talana, C.A., Yang, E.S., Chen, M., et al. (2022). Structural basis for potent antibody neutralization of SARS-CoV-2 variants including B.1.1.529. Science *376*, eabn8897. https://doi.org/10.1126/science.abn8897.

STAR★METHODS

KEY RESOURCES TABLE

REAGENT or RESOURCE	SOURCE	IDENTIFIER
Antibodies		
ACE2	(Henderson et al., 2020)	N/A
CR3022	(Henderson et al., 2020)	N/A
2G12	(Williams et al., 2021)	N/A
Goat anti-rabbit-HRP	Abcam	ab97080
Goat anti-human-HRP	Jackson ImmunoResearch Laboratories	109-035-098
Mouse anti-monkey IgG HRP	Southern Biotech	Cat #:4700-05; RRID:AB_2796069
DH1050.1	(Li et al., 2021)	N/A
DH1052	(Li et al., 2021)	N/A
S309	(Pinto et al., 2020)	N/A
DH1041	(Li et al., 2021)	N/A
DH1042	(Li et al., 2021)	N/A
DH1047	(Li et al., 2021)	N/A
S2X259	(Totorici et al., 2021)	N/A
DH1044	(Li et al., 2021)	N/A
DH1193	(Li et al., 2021)	N/A
DH1058	(Li et al., 2021)	N/A
Bacterial and virus strains		
Spike-pseudotyped virus D614G (B.1)	David Montefiori & Xiaoying Shen, Duke	
Spike-pseudotyped virus Omicron (B.1.1.529.1)	David Montefiori & Xiaoying Shen, Duke	
Spike-pseudotyped virus Omicron (B.1.1.529.2)	David Montefiori & Xiaoying Shen, Duke	
Spike-pseudotyped virus Omicron (B.1.1.529.3)	David Montefiori & Xiaoying Shen, Duke	
Chemicals, peptides, and recombinant proteins		
FreeStyle 293 Expression Medium	GIBCO	12,338,018
Expi293 Expression Medium	GIBCO	A1435101
ExpiFectamine 293 Transfection Kit	GIBCO	A14524
Hyclone SFM4HEK293	Cytiva	SH30521.02
Opti-MEM I	GIBCO	31,985-070
Turbo293	Speed BioSystems	PXX1002
10x Buffer E	IBA	2-1000
10x Buffer R	IBA	2-1002
10x Buffer W	IBA	2-1003
Strep-Tactin resin	IBA	2-1201
8% Glutaraldehyde	Electron Microscopy Sciences	16,019
300mesh Cu carbon coated	Electron Microscopy Sciences	CF300-Cu
Uranyl formate	Electron Microscopy Sciences	22,450 S-888
Quantifoil R 1.2/1.3 300 mesh	Electron Microscopy Sciences	Q350CR-14
Streptavidin	Thermo Fisher Scientific	S-888
Streptavidin-HRP	Thermo Scientific	Ref #21132
D-mannose	Sigma	CAS #:3458-28-4
Tween 20	Sigma	P7949

(*Continued on next page*)

Continued

REAGENT or RESOURCE	SOURCE	IDENTIFIER
Phosphate Buffered Saline (25x) pH 7.6	Cat No:	PBS-20000
Sodium Bicarbonate	Sigma	S6297
Sodium Azide	Sigma	S8032
Hydrochloric Acid	Fischer Scientific	A142-212
Whey Protein	Bipro USA	Unflavored Whey
Goat Serum	Invitrogen	16,210-072
SureBlue Reserve TMB	KPL	53-00-03
BSA	Sigma	A3059
HBS-EP + buffer 10x	Cytiva	BR100669
Critical commercial assays		
Superose 6 Increase 10/300 GL	Cytiva	29,091,596
NuPage 4-12%	Invitrogen	NP0321
TMB substrate	Sera Care Life Sciences	5120-0083
Luciferase Cell Culture Lysis 5x Reagent	Promega	Cat# E1531
Bright-Glo Luciferase Assay System	Promega	Cat# #2650
Series S CM5 Sensor chip	Cytiva	29,104,988
Series S SA sensor chip	Cytiva	BR100398
Human Antibody Capture kit	Cytiva	BR100839
Deposited data		
SARS-CoV-2 Omicron-BA.2 3-RBD down Spike Protein Trimer without the P986-P987 stabilizing mutations (S-GSAS-Omicron-BA.2)	This study	PDB 7UB0; EMDB- 26,433
SARS-CoV-2 Omicron-BA.2 3-RBD down Spike Protein Trimer without the P986-P987 stabilizing mutations (S-GSAS-Omicron-BA.2)	This study	PDB 7UB5; EMD- 26435
SARS-CoV-2 Omicron-BA.2 3-RBD down Spike Protein Trimer without the P986-P987 stabilizing mutations (S-GSAS-Omicron-BA.2)	This study	PDB 7UB6; EMD- 26436
SARS-CoV-2 Omicron-BA.2 1-RBD-up Spike Protein Trimer without the P986-P987 stabilizing mutations (S-GSAS-Omicron-BA.2)	This study	EMD- 26644
SARS-CoV-2 Omicron-BA.2 1-RBD-up Spike Protein Trimer without the P986-P987 stabilizing mutations (S-GSAS-Omicron-BA.2)	This study	EMD- 26647
SARS-CoV-2 Omicron-BA.2 1.5-RBD up Spike Protein Trimer without the P986-P987 stabilizing mutations (S-GSAS-Omicron-BA.2)	This study	EMD-26643
Experimental models: Cell lines		
Freestyle 293-F cells	GIBCO	R79007
Expi293F cells	GIBCO	A14527
293T/ACE2 cells	Drs. Mike Farzan and Huihui Mu, Scripps	N/A
HEK293T/17	ATCC	CRL-11268
Recombinant DNA		
pαH-S-GSAS/D614G	(Gobeil et al., 2021a)	Addgene 164,566
paH-S-GSAS-OMICRON-BA.1	(Gobeil et al., 2022)	Addgene 180,423
paH-S-GSAS-OMICRON-BA.2	This study	Addgene 184,829
paH-S-GSAS-OMICRON-BA.2-RBD	This study	Addgene 184,830
paH-S-GSAS-OMICRON-BA.1-RBD	This study	Addgene 184,831

(*Continued on next page*)

Continued

REAGENT or RESOURCE	SOURCE	IDENTIFIER
Software and algorithms		
Relion	(Scheres, 2012, 2016)	Version 3.1
cryoSPARC	(Punjani et al., 2017)	https://cryosparc.com
Phenix	(Afonine et al., 2018; Liebschner et al., 2019)	Version 1.17
Coot	(Emsley et al., 2010)	Version 0.8.9.2
Pymol	Schrodinger The PyMOL Molecular Graphics System (Schrödinger, 2015).	https://www.pymol.org/
UCSF Chimera	(Pettersen et al., 2004)	http://www.cgl.ucsf.edu/chimera/
Chimera X	(Goddard et al., 2018)	https://www.rbvi.ucsf.edu/chimerax/
Image Lab	Bio-Rad	Version 6.0
PRISM 8	GraphPad Software	Version 8.4.0
R	R Core Team (2014). R: A language and environment for statistical computing. R Foundation for Statistical Computing, Vienna, Austria. URL http://www.R-project.org/	version 4.0.2
Softmax Pro	Molecular Devices	Version 5.3
Bio3D	(Grant et al., 2020)	Version 2.4-1
ImageJ	(Schneider et al., 2012)	Version 1.53a
Sequencher (Version 5.4.6)	Gene Codes Corporation	www.Genecodes.com

RESOURCE AVAILABILITY

Lead contact

Further information and requests for resources and reagents should be directed to and will be fulfilled by the lead contact, Priyamvada Acharya (priyamvada.acharya@duke.edu).

Materials availability

Further information and requests for resources and reagents should be directed to Priyamvada Acharya (priyamvada.acharya@duke.edu). Plasmids generated in this study have been deposited to Addgene with the following accession numbers: 184,829, 184,830, 184,831.

Data and code availability

- Cryo-EM reconstructions and atomic models generated during this study are available at wwPDB and EMBD (https://www.rcsb.org; http://emsearch.rutgers.edu) under the accession codes PDB IDs 7UB0, 7UB5, 7UB6, and EMDB IDs 26433, 26435, 26436, 26643 and 26647.
- This paper does not report original code.
- Any additional information required to reanalyze the data reported in this paper is available from the lead contact upon request.

EXPERIMENTAL MODEL AND SUBJECT DETAILS

Cell culture

Gibco FreeStyle 293-F cells (embryonal, human kidney) were incubated at 37°C and 9% CO_2 in a humidified atmosphere. Cells were incubated in FreeStyle 293 Expression Medium (Gibco) with agitation at 120 rpm. Plasmids were transiently transfected into cells using Turbo293 (SpeedBiosystems) and incubated at 37°C, 9% CO2, 120 rpm for 6 days. On the day following transfection, HyClone CDM4HEK293 media (Cytiva, MA) was added to the cells.

Antibodies were produced in Expi293 cells (embryonal, human kidney). Cells were incubated in Expi293 Expression Medium at 37°C, 120 rpm and 8% CO_2 in a humidified atmosphere. Plasmids were transiently transfected into cells using the ExpiFectamine 293 Transfection Kit and protocol (Gibco).

METHOD DETAILS

Plasmids

Site-directed mutagenesis were performed and sequences confirmed by GeneImmune Biotechnology (Rockville, MD). The SARS-CoV-2 spike protein ectodomain constructs comprised the S protein residues 1 to 1208 (GenBank: MN908947) with the D614G mutation, the furin cleavage site (RRAR; residue 682-685) mutated to GSAS, a C-terminal T4 fibritin trimerization motif, a C-terminal HRV3C protease cleavage site, a TwinStrepTag and an 8XHisTag. All spike ectodomains were cloned into the mammalian expression vector pαH. The WT RBD construct obtained from BEI resources (Catalog number NR-52309) expressed the receptor binding domain (RBD) of the spike (S) glycoprotein gene from severe acute respiratory syndrome-related coronavirus 2 (SARS-CoV-2), Wuhan-Hu-1 (GenBank: MN908947) with an N-terminal S protein signal sequence to the spike RBD (amino acids 319 to 541) and a C-terminal 6X-histidine tag. The sequence was codon optimized for mammalian expression and subcloned into the pCAGGS mammalian expression vector under the AG promoter. All plasmids generated in this study have been deposited to Addgene (https://www.addgene.org).

Protein purification

Spike ectodomains were harvested from the concentrated supernatant on day 6 post transfection. The spike ectodomains were purified using StrepTactin resin (IBA LifeSciences) and size exclusion chromatography (SEC) using a Superose 6 10/300 GL Increase column (Cytiva, MA) equilibrated in 2 mM Tris, pH 8.0, 200 mM NaCl, 0.02% NaN_3. All purification steps were performed at room temperature within a single day. Protein quality was assessed by SDS-PAGE using NuPage 4-12% (Invitrogen, CA). The purified proteins were flash frozen and stored at −80°C in single-use aliquots. Each aliquot was thawed by a 20-min incubation at 37°C before use.

RBD variants were harvested from concentrated supernatant on the 6th day post transfection. The RBDs containing an 6x-Histidine tag were purified via nickel affinity chromatography using a HisTrap excel column (Cytiva, MA). Concentrated supernatant was loaded onto the column and the column washed with buffer A (1x PBS pH 8.0) until baseline. The proteins were eluted from the column by applying a gradient over 40 CV from 100% buffer A to 100% buffer B (1x PBS pH 8.0, 1 M Imidazole). Fractions containing RBD were pooled, concentrated, and further purified by size exclusion chromatography (SEC) using a Superdex 200 Increase 10/300 GL column (Cytiva, MA) equilibrated with 1x PBS, pH 8.0. All steps of the purification were performed at room temperature. Protein quality was assessed by SDS-PAGE using NuPage 4-12% (Invitrogen, CA). The purified proteins were flash frozen and stored at −80°C in single-use aliquots. Each aliquot was thawed at 4°C before use.

Antibodies were produced in Expi293F cells and purified by Protein A affinity and digested using LysC to generate Fab fragments. ACE2 with human Fc tag was purified by Protein A affinity chromatography and SEC.

Differential scanning fluorimetry

DSF assays were performed using Tycho NT.6 (NanoTemper Technologies). Spike ectodomains were diluted to approximatively 0.15 mg/mL. Intrinsic fluorescence was measured at 330 nm and 350 nm while the sample was heated from 35 to 95°C at a rate of 30°C/min. The ratio of fluorescence (350/330 nm) and inflection temperatures (T_i) were calculated using the inbuilt software in the Tycho NT. 6.

ELISA assays

Spike ectodomains were tested for antibody- or ACE2-binding in ELISA assays as previously described (Edwards et al., 2021). Serially diluted spike protein was bound in wells of a 384-well plates, which were previously coated with streptavidin (Thermo Fisher Scientific, MA) at 2 μg/mL and blocked. Proteins were incubated at room temperature for 1 h, washed, then human mAbs were added at 10 μg/mL. Antibodies were incubated at room temperature for 1 h, washed and binding detected with goat anti-human-HRP (Jackson ImmunoResearch Laboratories, PA) and TMB substrate.

Recombinant FDG mAbs were tested for binding to the SARS-CoV-2 spikes in ELISA. Briefly, spike proteins (20 ng) were captured by streptavidin (30 ng per well) to individual wells of a 384-well Nunc-absorb ELISA plates using PBS-based buffers and assay conditions as previously described (PMID: 34019795; PMID: 28298421; PMID: 28298420). Commercially obtained D-mannose (Sigma, St. Louis, MO) was used to outcompete mAb binding to glycans on the spike proteins; D-mannose solutions were also produced in ELISA PBS-based glycan buffers at a concentration of [1M] D-mannose as described (PMID: 34019795). Mouse anti-monkey IgG-HRP (Southern Biotech, CAT# 4700-05) and Goat anti-human IgG-HRP (Jackson ImmunoResearch Laboratories, CAT# 109-035-098) secondary antibodies were used to detect antibody bound to the spike proteins. HRP detection was subsequently quantified with 3,30,5,50-tetramethylbenzidine (TMB) by measuring binding levels at an absorbance of 450nm, and binding titers were also reported as Log area under the curve (AUC).

Surface plasmon resonance

Binding experiments were performed using SPR on a Biacore T-200 (Cytiva, MA, formerly GE Healthcare) with HBS buffer supplemented with 3 mM EDTA and 0.05% surfactant P-20 (HBS-EP+, Cytiva, MA). All binding assays were performed at 25°C.

Spike variants were captured on a Series S Strepavidin (SA) chip (Cytiva, MA) coated at 200 nM (120 s at 5 μL/min). Fabs were injected at concentrations ranging from 0.5 nM to 8 nM (prepared in a 2-fold serial dilution manner) over the S proteins using the single cycle kinetics mode with 5 concentrations per cycle. The surface was regenerated after the last injection with 3 pulses of a 50 mM NaoH + 1M NaCl solution for 10 s at 100 μL/min.

RBD binding to IgG's was assessed using a Series S CM5 chip (Cytiva, MA) which was labeled with anti-human IgG (fc) antibody using a Human Antibody Capture Kit (Cytiva, MA). IgGs were then coated at 200 nM (120 s at 5 μL/min). RBDs were injected at concentrations ranging from 0.5 nM to 40 nM (prepared in a 2-fold serial dilution manner) over the antibodies using the single cycle kinetics mode with 5 concentrations per cycle. The surface was regenerated after the last injection with 3 pulses of a 3 M $MgCl_2$ solution for 10 s at 100 μL/min.

Sensogram data were analyzed using the BiaEvaluation software (Cytiva, MA)

Cryo-EM

Purified SARS-CoV-2 spike ectodomains were diluted to a concentration of ~1.5 mg/mL in 2 mM Tris pH 8.0, 200 mM NaCl and 0.02% NaN_3 and 0.5% glycerol was added. A 2.3-μL drop of protein was deposited on a Quantifoil-1.2/1.3 grid (Electron Microscopy Sciences, PA) that had been glow discharged for 10 s using a PELCO easiGlow Glow Discharge Cleaning System. After a 30 s incubation in >95% humidity, excess protein was blotted away for 2.5 s before being plunge frozen into liquid ethane using a Leica EM GP2 plunge freezer (Leica Microsystems). Frozen grids were imaged using a Titan Krios (Thermo Fisher) equipped with a K3 detector (Gatan). The cryoSPARC (Punjani et al., 2017) software was used for data processing. Phenix (Liebschner et al., 2019; Afonine et al., 2018), Coot (Emsley et al., 2010), Pymol (Schrodinger, 2015), Chimera (Pettersen et al., 2004), ChimeraX (Goddard et al., 2018) and Isolde (Croll, 2018) were used for model building and refinement.

Vector based structure analysis

Vector analysis of intraprotomer domain positions was performed as described previously (Henderson et al., 2020) using the Visual Molecular Dynamics (VMD) (Humphrey et al., 1996) software package Tcl interface. Alpha carbons of each S1 protomer domain and the S2 CD and an S2 sheet motif were used to determine domain centroids for vector calculations. Vectors connecting structurally related domain centroids were used to calculate relevant distances, angles, and dihedrals. Principal components analysis and K-means clustering of the vector sets was performed in R (Team, 2017). Data were centered and scaled for the PCA analyses. Principal components analysis, K-means clustering, and Pearson correlation (confidence interval 0.95, $p < 0.05$) analysis of vectors sets was performed in R. Data were centered and scaled for the PCA analyses. The structures used in this analysis included PDB IDs 7KE8 ($G614^1$), 7KE6 ($G614^2$), 7KE7 ($G614^3$), 7KE4 ($G614^4$), 7LWS (Alpha), 7LYL (Beta), 8CSA (TM), 7LWL (Mk1), 7LWI (Mk2), 7LWK (Mk3), 7LWJ (Mk4), 7TOU (D1), 7TOX (D5), 7TOY (D6), 7TOZ (D7), 7TP0 (D8), 7TP1 (D9), 7TP2 (D10), 7TF8 (BA.1 State 1), 7TL1 (BA.1 State 2), 7UB0 (BA.2 State 1), 7UB5 (BA.2 State 2) and 7UB6 (BA.2 State 3).

Difference distance matrices (DDM)

DDM were generated using the Bio3D package (Grant et al., 2020) implemented in R (R Core Team (2014). R: A language and environment for statistical computing. R Foundation for Statistical Computing, Vienna, Austria. URL http://www.R-project.org/)

Pseudovirus neutralization assay

The pseudovirus neutralization assay performed at Duke has been described in detail (Gilbert et al., 2022) and is a formally validated adaptation of the assay utilized by the Vaccine Research Center; the Duke assay is FDA approved for D614G. For measurements of neutralization, pseudovirus was incubated with 8 serial 5-fold dilutions of antibody samples (1:20 starting dilution using antibodies diluted to 1.0 mg/mL) in duplicate in a total volume of 150 μL for 1 h at 37°C in 96-well flat-bottom culture plates. 293T/ACE2-MF cells were detached from T75 culture flasks using TrypLE Select Enzyme solution, suspended in growth medium (100,000 cells/mL) and immediately added to all wells (10,000 cells in 100 μL of growth medium per well). One set of 8 wells received cells + virus (virus control) and another set of 8 wells received cells only (background control). After 71-73 h of incubation, medium was removed by gentle aspiration and 30 μL of Promega 1X lysis buffer was added to all wells. After a 10-min incubation at room temperature, 100 μL of Bright-Glo luciferase reagent was added to all wells. After 1-2 min, 110 μL of the cell lysate was transferred to a black/white plate. Luminescence was measured using a GloMax Navigator luminometer (Promega). Neutralization titers are the inhibitory dilution (ID) of serum samples at which RLUs were reduced by 50% (ID50) compared to virus control wells after subtraction of background RLUs. Serum samples were heat-inactivated for 30 min at 56°C prior to assay.

Immunoprecipitation assays

For each time point and controls, 20 μL of 50% slurry Protein A-agarose resin was spun down for 3 min at 500 G. The supernatant was then removed and 3 washes with 100 μL of PBS were performed with spins of 3 min at 3,000 G to precipitate the resin. 10 μL of PBS was then added to the resin, followed by 5 μg of the antibody (DH1058, DH1294, or PGT145 for the control) and 5 μg of each spike protein. The combinations were incubated at room temperature according to the time points. To stop the reaction, following 3 washes of the resin with 100 μL of PBS as described above, the washed resin was resuspended in 10 μL of 4x loading buffer (BioRad) containing DTT and boiled at 95°C for 5 min. The samples were then flash-frozen until ready to be loaded on an SDS-PAGE using NuPage 4-12% (Invitrogen, CA). Gel staining was done using the SimplyBlue SafeStain (ThermoFisher) and gel imaging was done using a ChemiDoc (BioRad). Quantification of the band intensity was done using the BioRad Image Lab Software.

QUANTIFICATION AND STATISTICAL ANALYSIS

Cryo-EM data were processed and analyzed using cryoSPARC. Cryo-EM structural statistics were analyzed with Phenix and Molprobity. Statistical details of experiments are described in method details or Figure Legends.

Cell Reports, Volume *39*

Supplemental information

Cryo-EM structures of SARS-CoV-2

Omicron BA.2 spike

Victoria Stalls, Jared Lindenberger, Sophie M.-C. Gobeil, Rory Henderson, Rob Parks, Maggie Barr, Margaret Deyton, Mitchell Martin, Katarzyna Janowska, Xiao Huang, Aaron May, Micah Speakman, Esther Beaudoin, Bryan Kraft, Xiaozhi Lu, Robert J. Edwards, Amanda Eaton, David C. Montefiori, Wilton B. Williams, Kevin O. Saunders, Kevin Wiehe, Barton F. Haynes, and Priyamvada Acharya

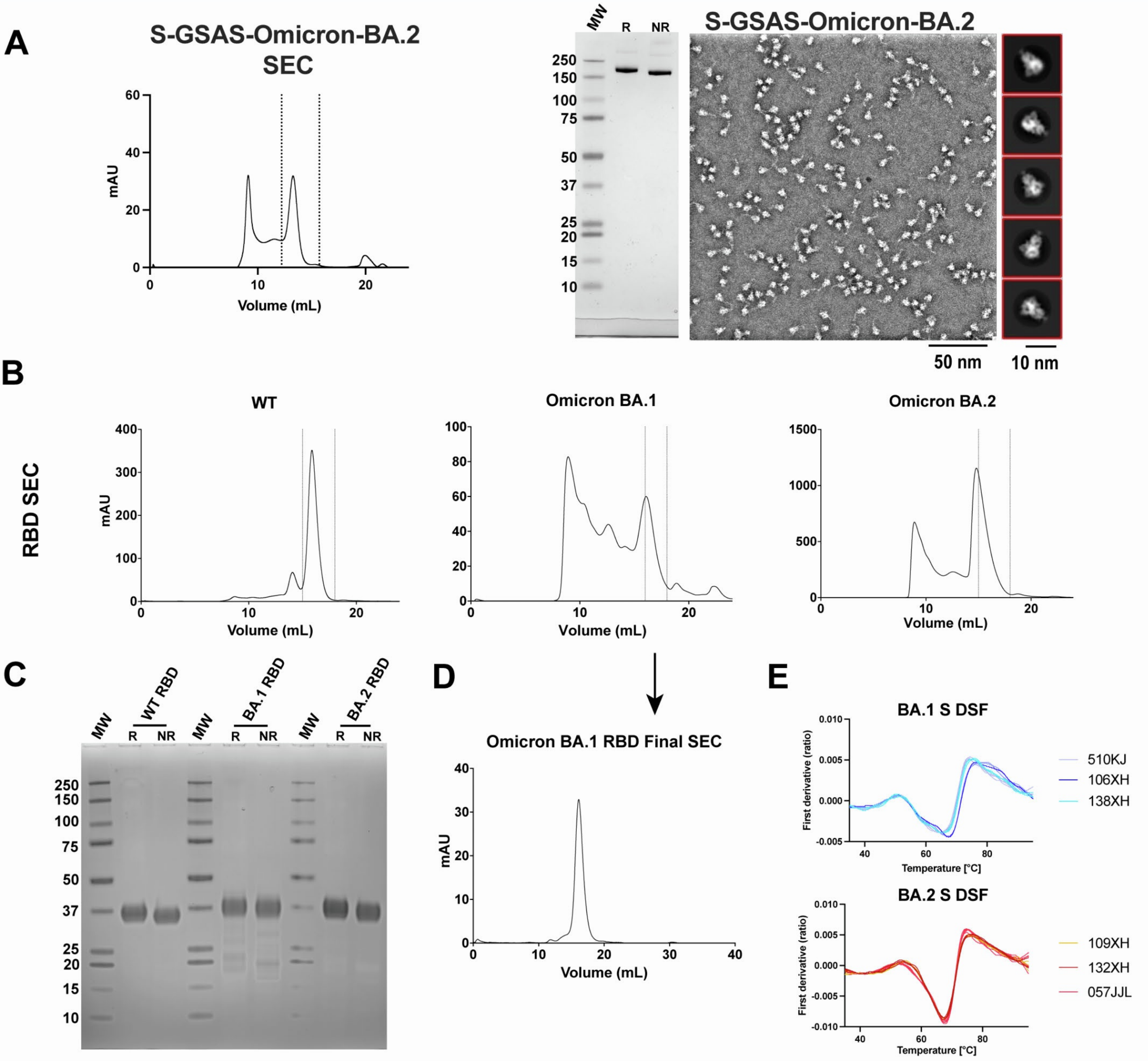

	Lot #	Ti#1 Mean ± St Dev	Ti#2 Mean ± St Dev	Ti#3 Mean ± St Dev
S-GSAS-Omicron-BA.1	510KJ	50.7 ± 0.1	64.9 ± 0.9	74.1 ± 0.3
	106XH	50.8 ± 0.2	67.4 ± 0.2	77.0 ± 0.9
	138XH	50.9 ± 0.9	65.4 ± 0.5	75.2 ± 0.6
S-GSAS-Omicron-BA.2	109XH	54.5 ± 0.4	67.5 ± 0.1	76.0 ± 0.8
	132XH	53.6 ± 0.6	67.4 ± 0.3	76.3 ± 0.5
	057JJL	52.5 ± 1.0	67.6 ± 0.2	74.9 ± 0.3

Figure S1. Quality control of SARS-CoV-2 S proteins and RBD proteins, Related to Figures 1 and 2. (A) S-GSAS-Omicron-BA.2: (left) Size Exclusion Chromatography (SEC) with dashed lines indicating peak fractions pooled for final sample. (middle-left) SDS-PAGE: lane 1 molecular weight marker, lane 2 Reduced (R), and Non-reduced (NR) of 2 μg Spike protein. (middle-right) Representative micrograph with 50 nm scale bar, and (right) 2D class averages with 10 nm scale bar. **(B)** From left to right SEC curves of WT, Omicron-BA.1, and Omicron-BA.2 RBDs, with dashed lines showing pooled fractions. **(C)** RBD protein SDS-PAGE with molecular weight marker, WT R and NR, Omicron-BA.1 R and NR, and Omicron-BA.2 R and NR. **(D)** Second and final SEC of Omicron-BA.1 RBD taken from pooled fractions indicated in B. **(E)** DSF plots of S-GSAS-Omicron BA.1 and BA.2 separated by lots. All lots were ran with three technical replicates, except 057JJL which had 6. Bottom table shows inflection temperatures ± standard deviation. *Fig 2A also includes data from lots 106XH and 109XH.

O$^{1}_{\mathrm{BA.2}}$ (PDB 7UB0; EMD-26433)

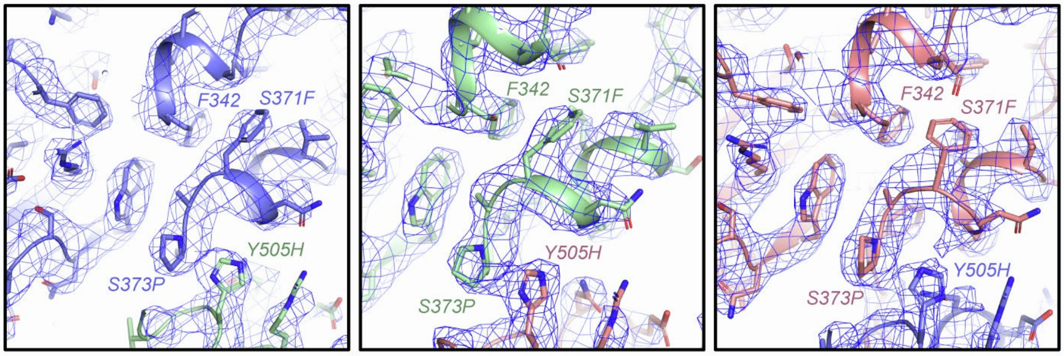

O$^{2}_{\mathrm{BA.2}}$ (PDB 7UB5; EMD-26435)

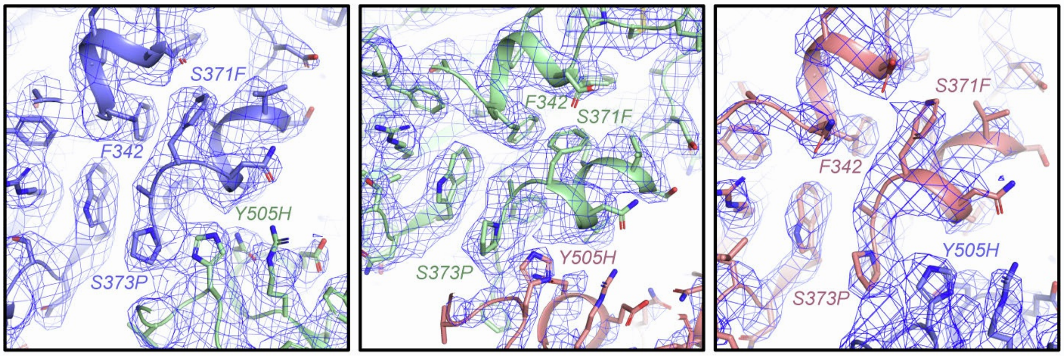

O$^{3}_{\mathrm{BA.2}}$ (PDB 7UB6; EMD-26436)

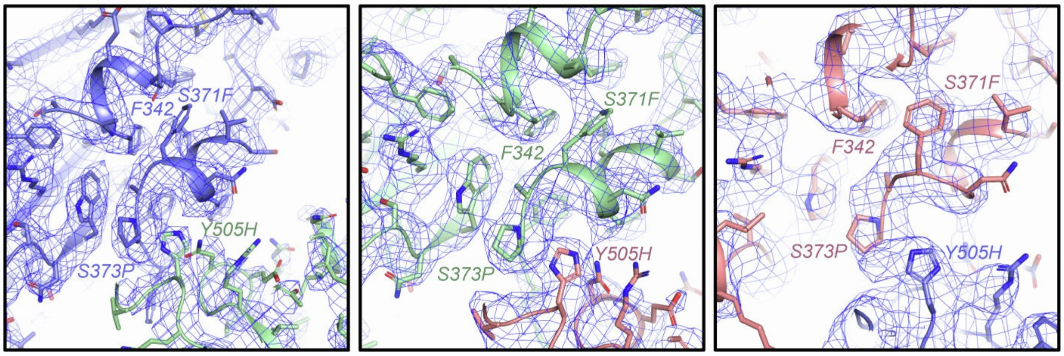

Figure S2. View of RBD interfacial region bearing S371F and S373P substitutions, Related to Figures 1 and 3. Cryo-EM reconstructions are shown as blue mesh with underlying fitted model in cartoon and side chains in sticks. Each panel shows the packing of the RBD region bearing the S371F and S373P substitutions with the RBD helix bearing residue F342, as well as inter-protomer packing with the adjacent RBD Y505H substitution stacking against P373. Details are shown for each protomer in O$^{1}_{\mathrm{BA.2}}$ (top row), O$^{2}_{\mathrm{BA.2}}$ (middle row) and O$^{3}_{\mathrm{BA.2}}$ (bottom row).

$O^1_{BA.2}$ (PDB 7UB0; EMD-26433)

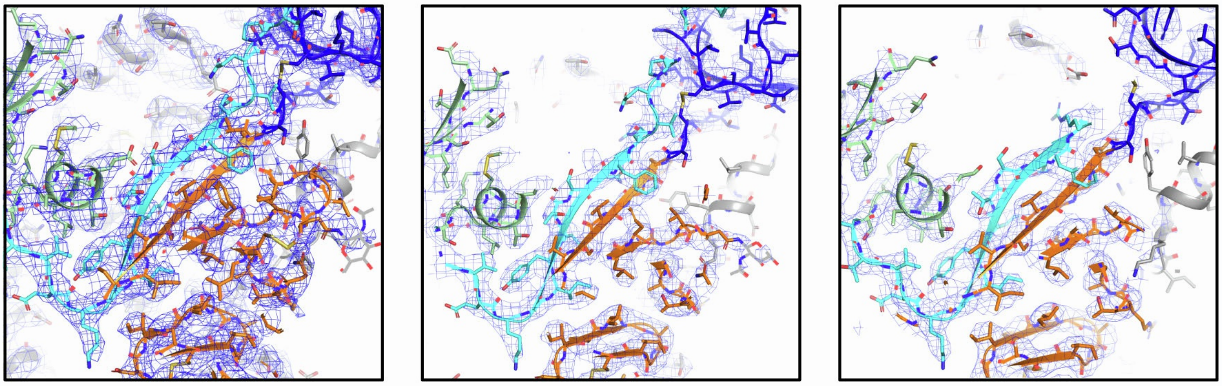

$O^2_{BA.2}$ (PDB 7UB5; EMD-26435)

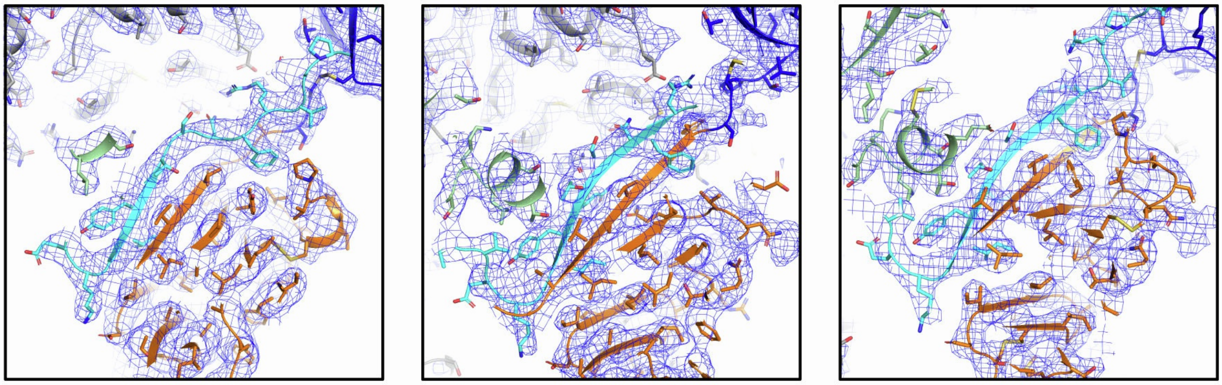

$O^3_{BA.2}$ (PDB 7UB6; EMD-26436)

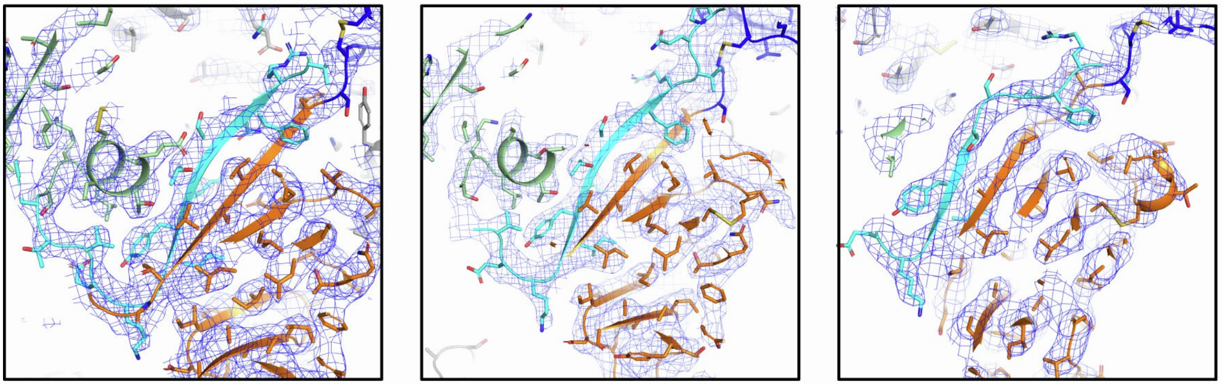

Figure S3. View of NTD-to-RBD (N2R) linker in 3-RBD-down Omicron BA.2 S, Related to Figure 4. Cryo-EM reconstructions are shown as blue mesh with underlying fitted model in cartoon and side chains in sticks. Each panel shows the N2R linker (cyan) of a protomer stacked against its SD2 subdomain (orange). The NTD is colored green and SD1 subdomain blue. Details are shown for each protomer in $O^1_{BA.2}$ (top row), $O^2_{BA.2}$ (middle row) and $O^3_{BA.2}$ (bottom row).

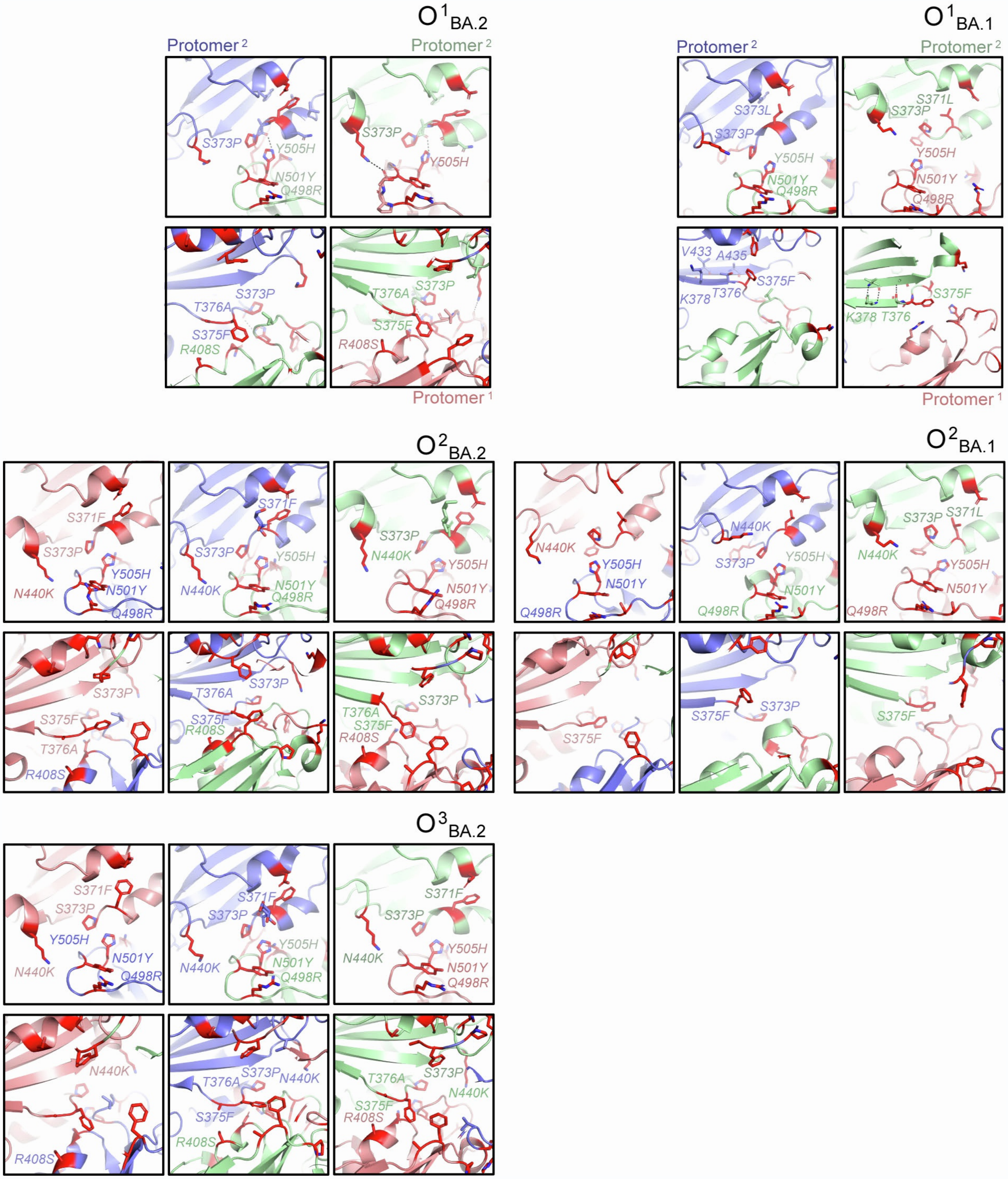

Figure S4. Comparison of the RBD-RBD interface in the Omicron BA.1 and BA.2 S 3-RBD-down structures, Related to Figure 3. Interprotomer interactions between adjacent RBDs are shown for (left) the BA.2 S protein structures (O$^{1}_{BA.2}$: PDB 7UB0; O$^{2}_{BA.2}$: PDB 7UB5; O$^{3}_{BA.2}$: PDB 7UB6), and (right) the BA.1 S protein structures (O$^{1}_{BA.1}$: PDB 7TF8; O$^{2}_{BA.1}$: PDB 7TL1)

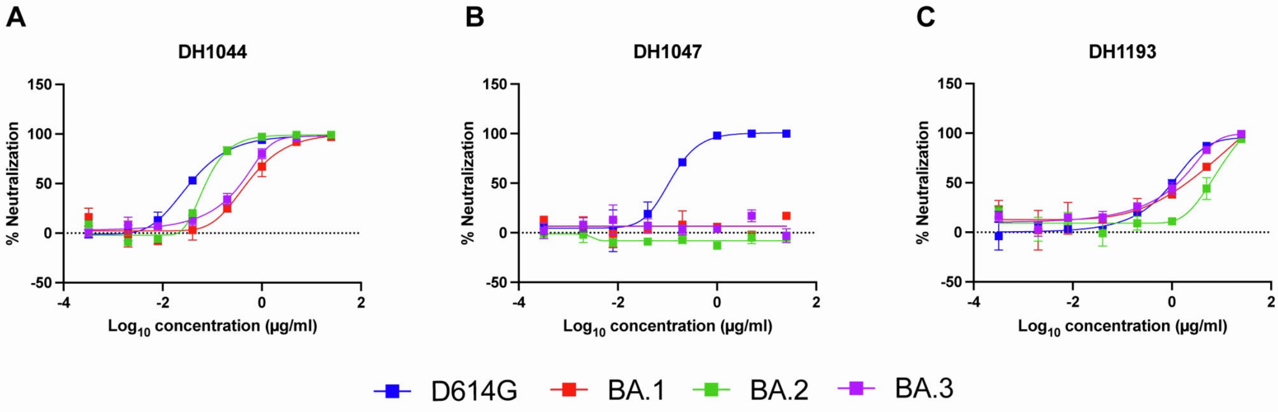

D

	D614G		Omicron -BA.1		Omicron -BA.2		Omicron -BA.3	
	ID50	ID80	ID50	ID80	ID50	ID80	ID50	ID80
DH1044	0.04	0.17	0.52	2.3	0.09	0.19	0.35	0.99
DH1047	0.1	0.34	>25	>25	>25	>25	>25	>25
DH1193	1	3.7	2	11	6.1	16	1.3	4.4

Figure S5. Pseudovirus neutralization by RBD-directed antibodies. Related to Figure 5. A. DH1044, **B.** DH1047, and **C.** DH1193. **D.** ID50 and ID80 values in µg/ml. Neutralization data are presented as the mean of 2 technical replicates within the same assay and the error bars indicate the percent difference between the duplicate wells at each dilution. The neutralization data were log transformed and then fitted with an asymmetric five-parameter curve within Graphpad Prism. The ID50 and ID80 values represent the antibody concentration necessary to achieve 50% and 80% neutralization of each virus tested.

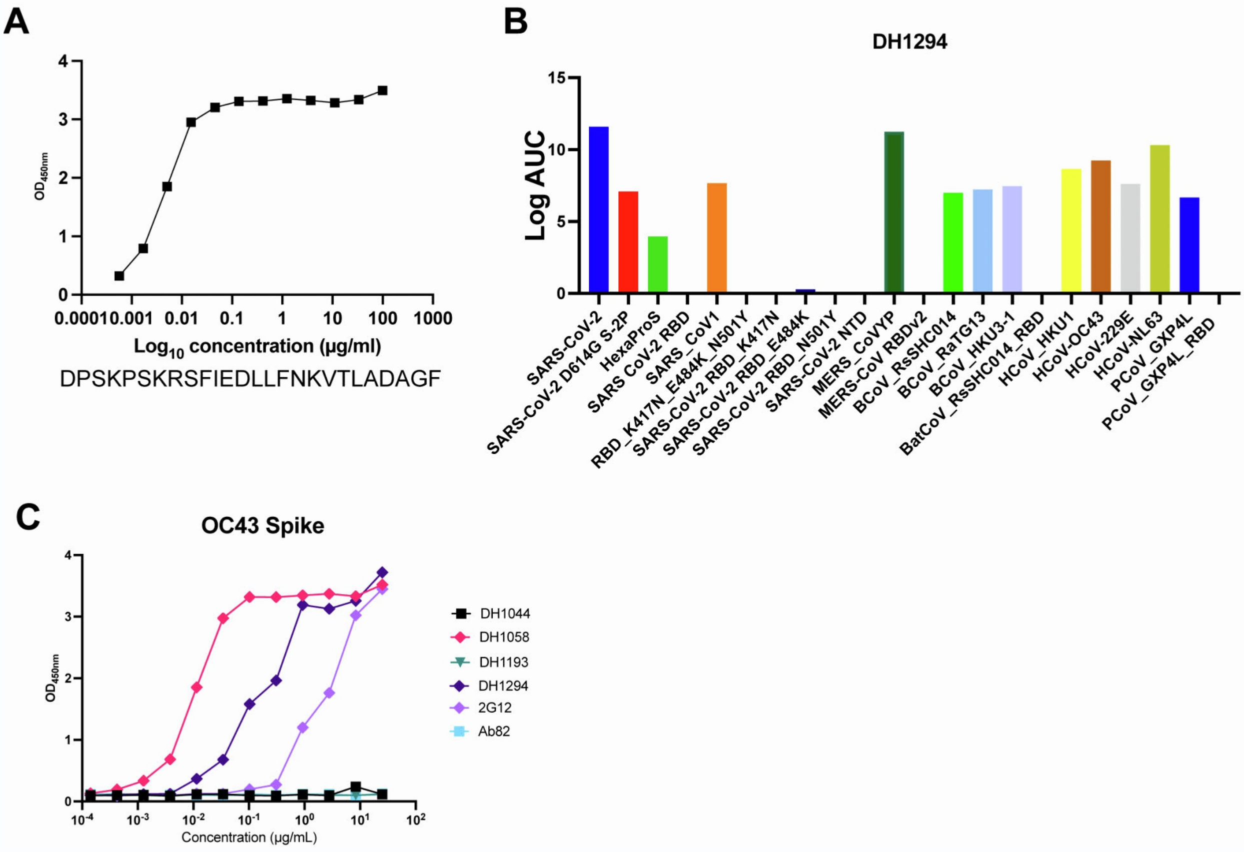

Figure S6. Epitope mapping of fusion peptide directed antibody DH1294, Related to Figure 7. A. Binding of antibody DH1294 to the fusion peptide (sequence indicated below)**. B.** ELISA binding of DH1294 to diverse CoV spikes. **C.** ELISA binding of antibodies to the CoV OC43 spike.

Table S1: Cryo-EM data collection and refinements statistics
S-GSAS-Omicron-BA.2, related to Figures 1, 3, 4, 6, 7, S2-S4, Data S2-S3.

	3-down			**1-up**		**1.5-up**
PDB ID	7UB0	7UB5	7UB6	n/a	n/a	n/a
EMDB ID	26433	26435	26436	26644	26647	26643
Data Collection and processing						
Microscope	FEI Titan Krios					
Detector	Gatan K3					
Magnification	81000					
Voltage (kV)	300					
Electron exposure (e-/Å^2)	54.7					
Defocus Range (µm)	2.6 to 0.8					
Pixel size (Å)	1.08					
Reconstruction software	cryoSPARC					
Symmetry imposed	C1	C1	C1	C1	C1	C1
Initial particle images (no.)						
Final particle images (no.)	411,890	276,707	198,211	70,271	114,624	54,450
Map resolution (Å)	3.31	3.35	3.52	3.93	3.74	3.98
FSC threshold	0.143	0.143	0.143	0.143	0.143	0.143
Refinement						
Initial model used	7KDK	7KDK	7KDK			
Model composition						
Nonhydrogen atoms	25,039	24,963	24,762			
Protein residues	3,112	3,107	3,105			
R.M.S. deviations						
Bond lengths (Å)	0.004	0.004	0.004			
Bond angles (°)	0.651	0.663	0.669			
Validation						
MolProbity score	1.22	1.29	1.24			
Clashscore	3.25	2.74	2.96			
Poor rotamers (%)	0	0	0			
EM ringer score	3.44	3.13	2.97			
Ramachandran plot						
Favored regions (%)	97.49	96.47	97.19			
Allowed (%)	2.51	3.53	2.81			
Disallowed regions (%)	0	0	0			

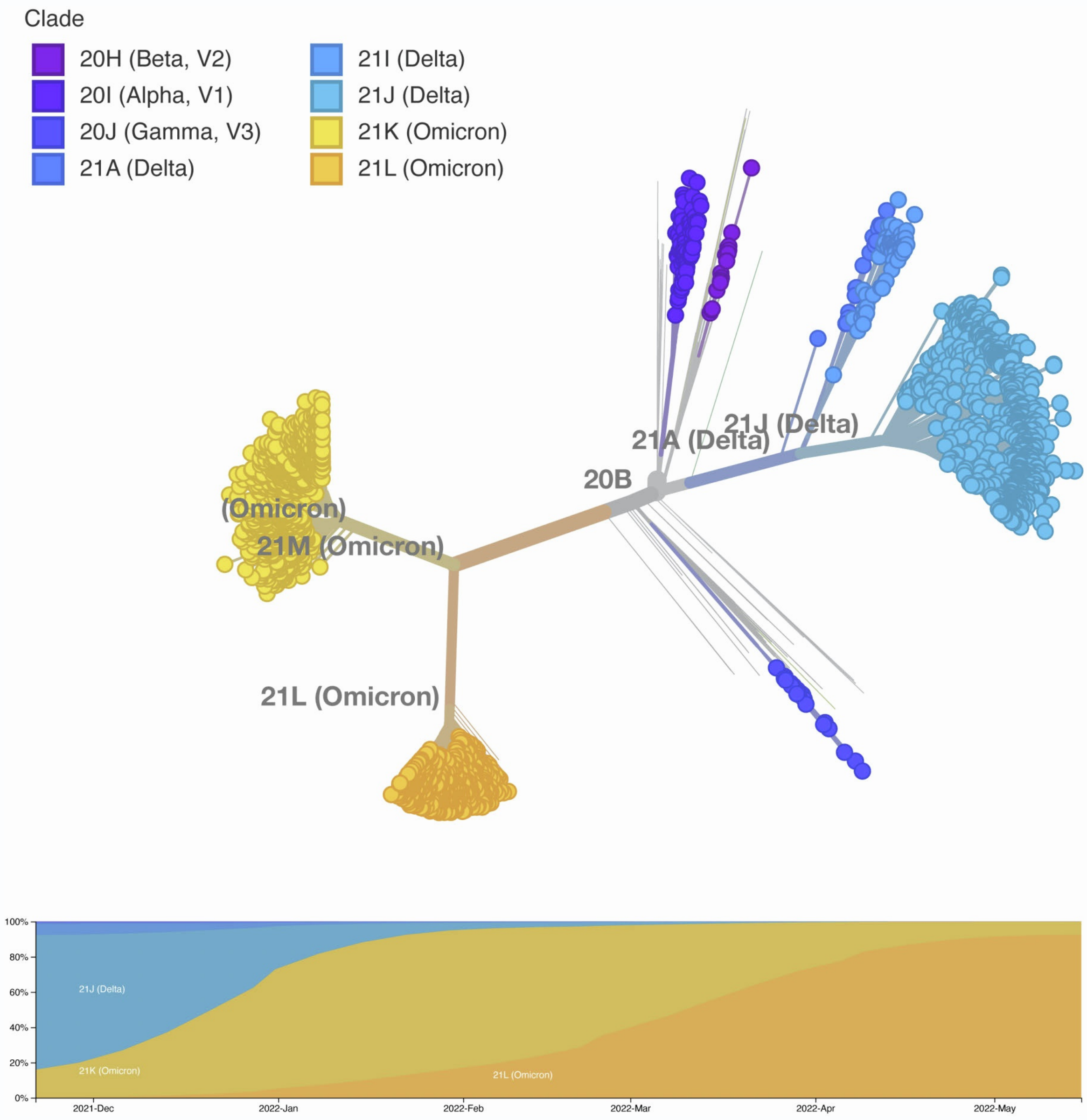

Data S1. Emergence and spread of the SARS-CoV-2 Omicron variant lineages, Related to Figure 1. Top. Phylogenetic tree of SARS-CoV-2 variants of concern. **Botttom.** Global frequencies of SARS-CoV-2 variants plotted against time from April 2021 to May 2022.

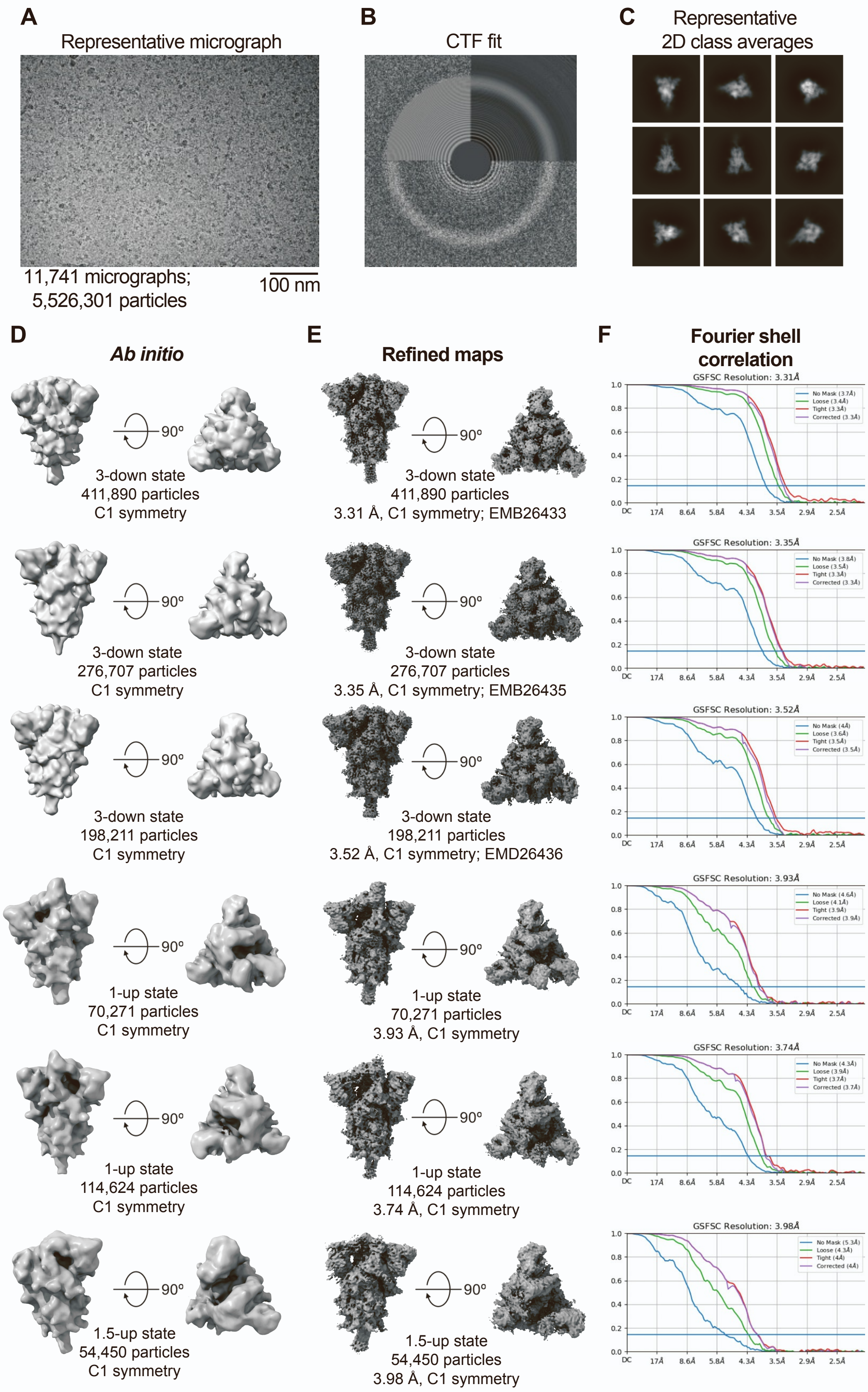

Data S2. Cryo-EM data processing for the S-GSAS-Omicron SARS-CoV-2 S ectodomain, Related to Figure 1, Table S1. **(A)** Representative micrograph. **(B)** CTF Fit. **(C)** Representative 2D class averages from cryo-EM dataset. Box size = 345.6 Å. **(D)** Ab initio reconstructions for the cryo-EM 3-RBD-down, 1-RBD-up, and 1.5-RBD-up states. **(E)** Refined maps for the cryo-EM corresponding states. **(F)** Fourier shell correlation curves for the cryo-EM corresponding states.

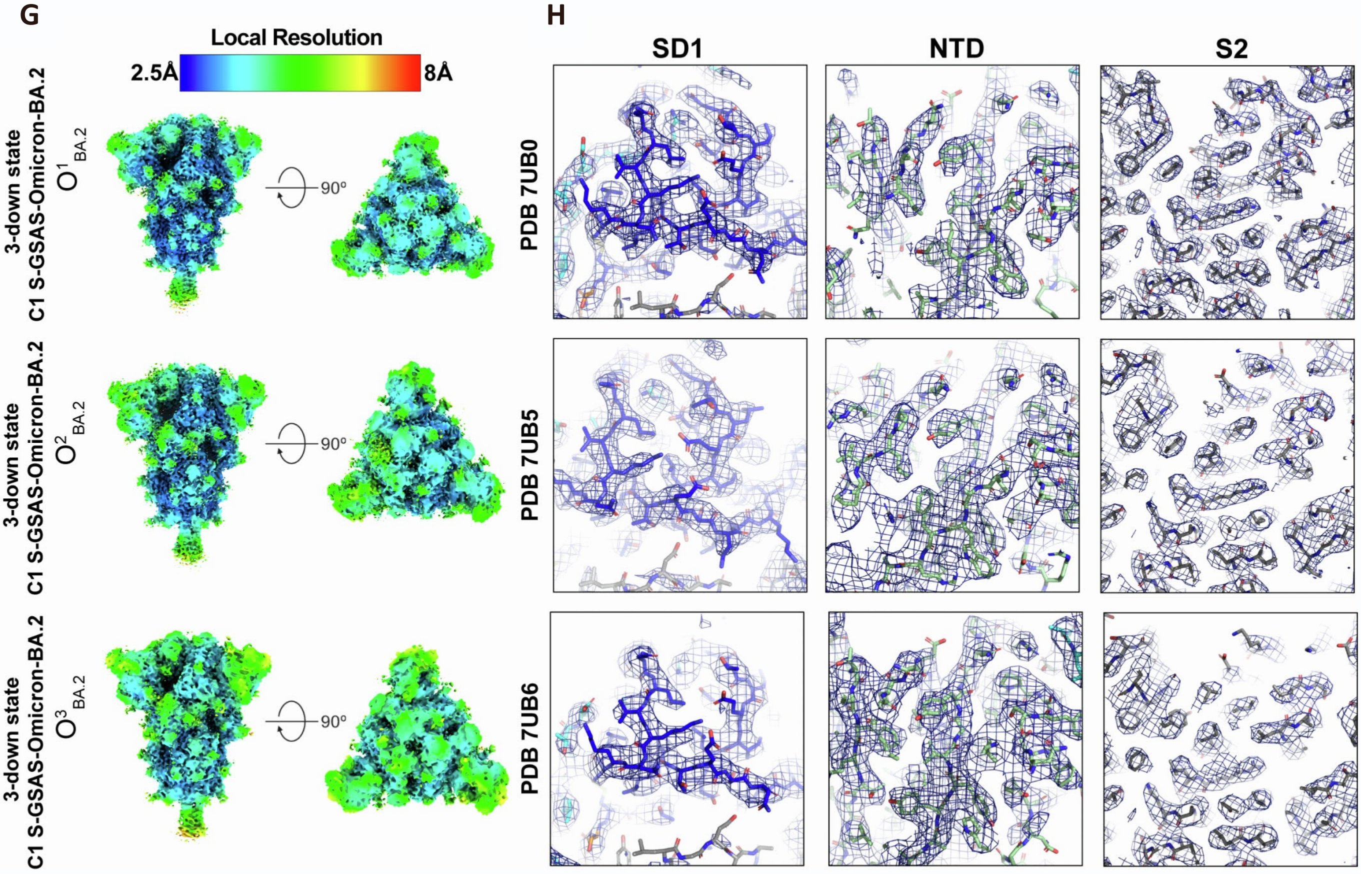

Data S2 continued. Cryo-EM data processing for the S-GSAS-Omicron SARS-CoV-2 S ectodomain, Related to Figure 1, Table S1. (G) Refined maps colored by local resolution ranging from 2.5 Å to 8 Å. **(H)** Zoomed in views of SD1, NTD, and S2.

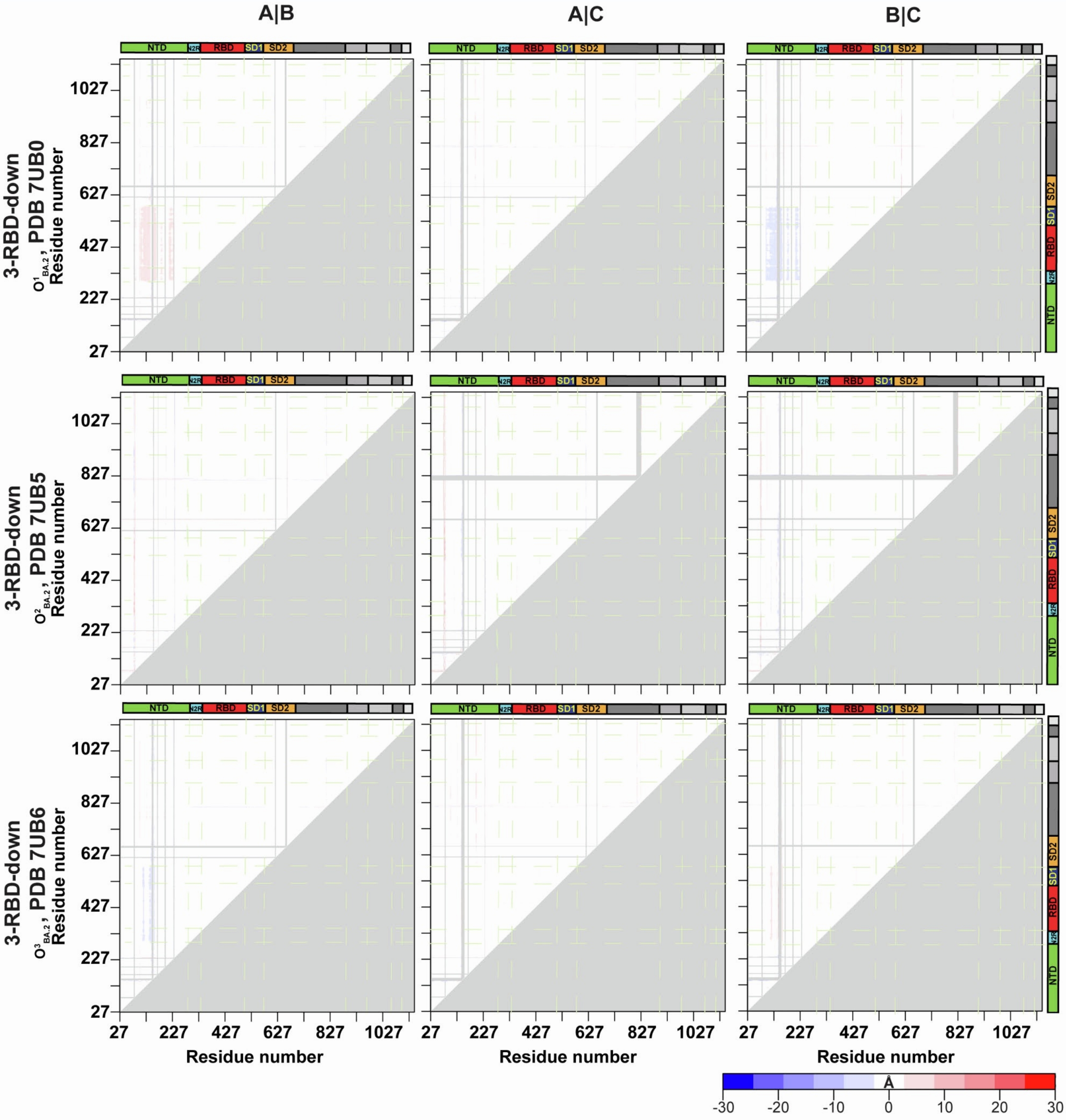

Data S3. Difference distance matrices (DDMs) analyses of S-GSAS-Omicron-BA.2 S ectodomain 3-RBD-down structures. Related to Figures 1 and 3, Table S1. Intrachain variability. Difference distance matrices (DDMs) provide superposition-free comparisons between a pair of structures by calculating the differences between the distances of each pair of Ca atoms in a structure and the corresponding pair of Ca atoms in the second structure. DDM of the 3-RBD down structures comparing each chain of a structure to the other chains of the same structure. The coloring scale used for the DDM analysis is represented on the bottom right corner.

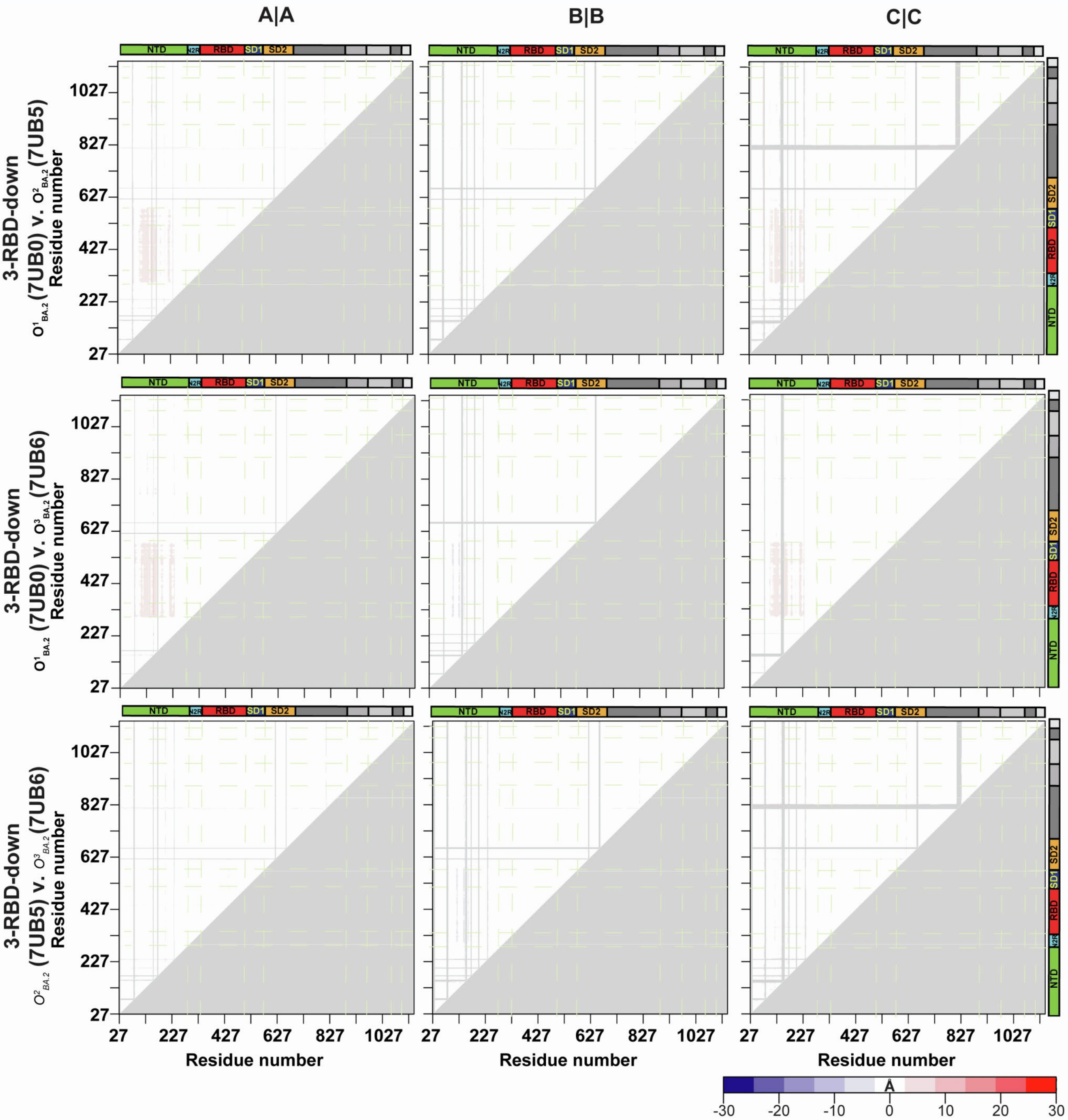

Data S3 continued. Difference distance matrices (DDMs) analyses of S-GSAS-Omicron-BA.2 S ectodomain 3-RBD-down structures. Related to Figures 1 and 3, Table S1. Interchain variability. DDM of the 3-RBD down structures comparing each chain of a structure to the same chain of another structure. The coloring scale used for the DDM analysis is represented on the bottom right corner.

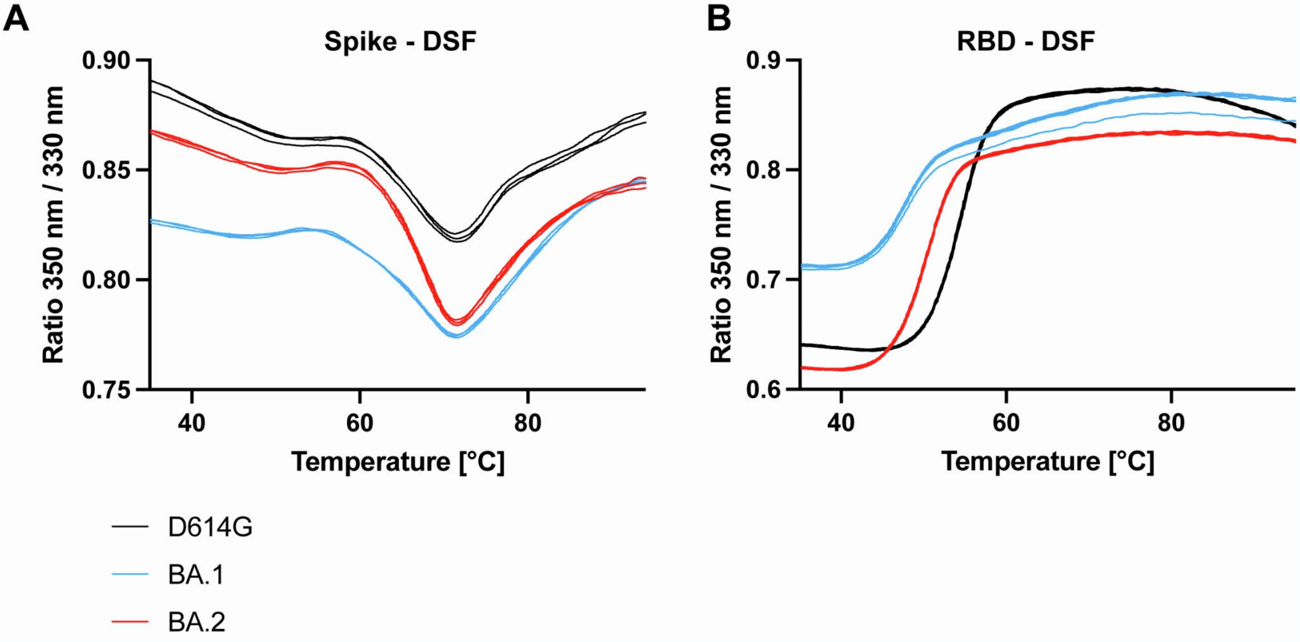

Data S4. Thermostability of SARS-CoV-2 S proteins and RBD proteins, Related to Figure 2. A. SARS-CoV-2 S protein DSF profiles showing changes in protein intrinsic fluorescence (expressed as a ratio between fluorescence at 350 and 330 nm). For each S protein construct (color coded as shown), three overlaid curves (technical replicates) are shown.

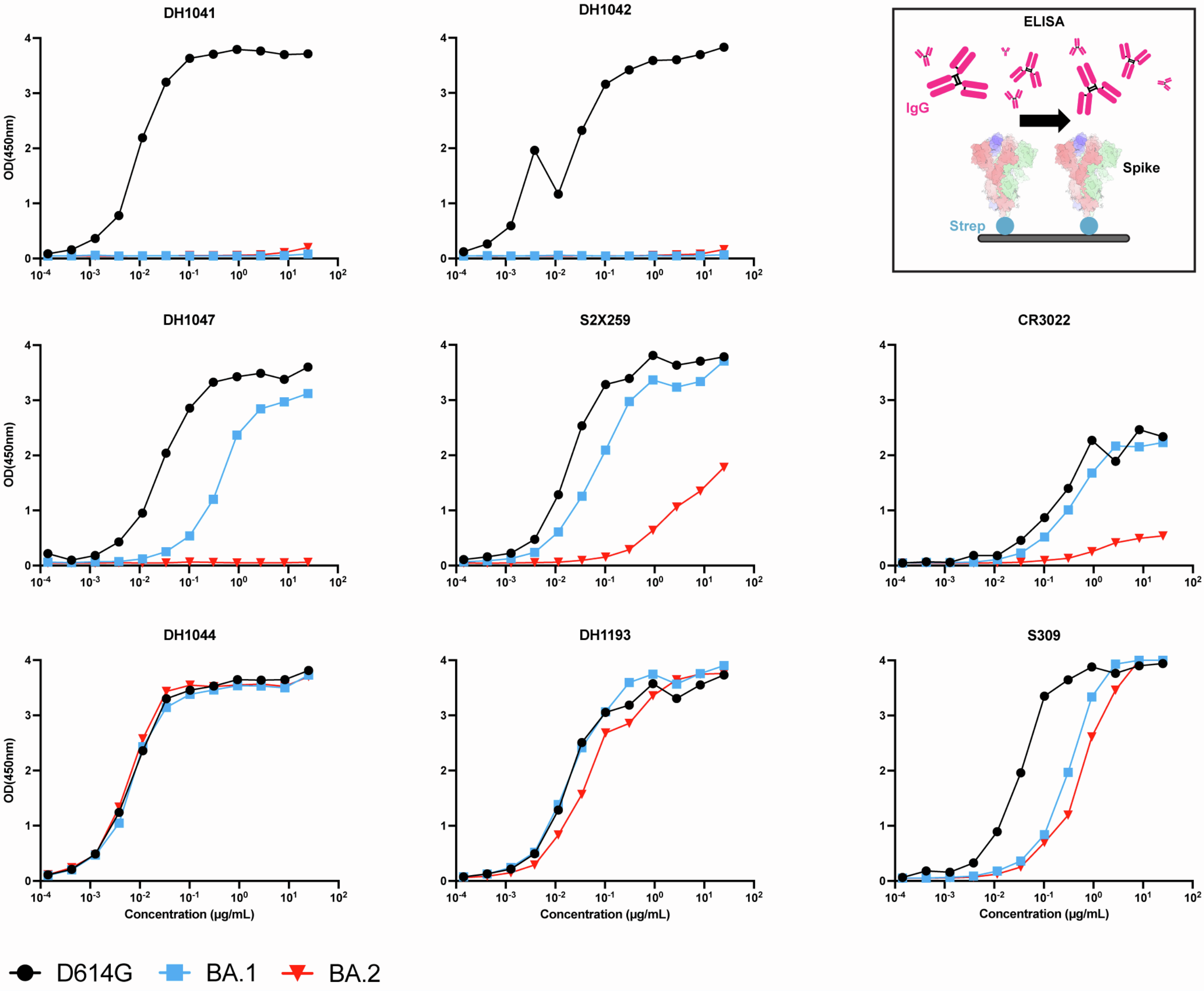

Data S5. Binding of RBD-directed antibodies to S protein and RBD variants, Related to Figures 5 and 6. ELISA binding of antibodies, top row, DH1041 and DH1042 (RBM-targeting), second row, DH1047, S2X259, and CR3022 (inner face RBD-targeting), and bottom row, DH1044, DH1193, and S309 (outer RBD face-targeting) to the D614G (black), BA.1 (blue) and BA.2 (red) S protein ectodomains. Schematic shows the assay format. Data are representative of at least two independent experiments.

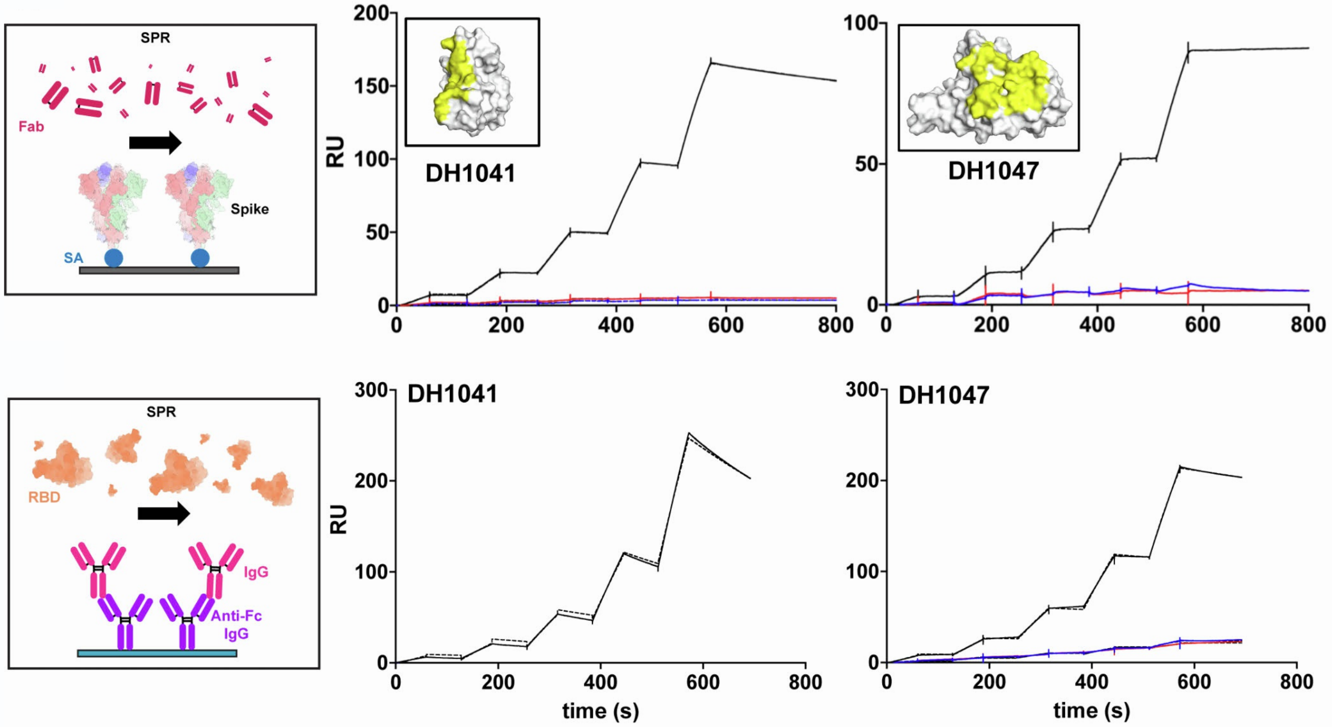

Data S5 continued. Binding of RBD-directed antibodies to S protein and RBD variants, Related to Figures 5 and 6. Binding of RBD-directed Fabs to S protein and RBD variants measured by SPR. **Top.** Schematic shows the assay format. Spike is captured on a Series S Streptavidin (SA) chip coated at 200 nM. Fabs were then injected at concentrations ranging from 0.5 nM to 8 nM, with a contact time of 60 seconds and a dissociation time of 120 seconds (50 µL/min)
Bottom. Schematic shows the assay format. Antibodies were captured on a CM5 chip labeled with anti-Fc IgG antibodies. Binding of DH1044 and DH1193 Fabs to D614G (black), BA.1 (blue) and BA.2 (red) S protein ectodomains measured by SPR. The solid lines are the binding sensograms; the dotted lines show fits of the data to a 1:1 Langmuir binding model. Data shown are representative of at least two independent experiments.

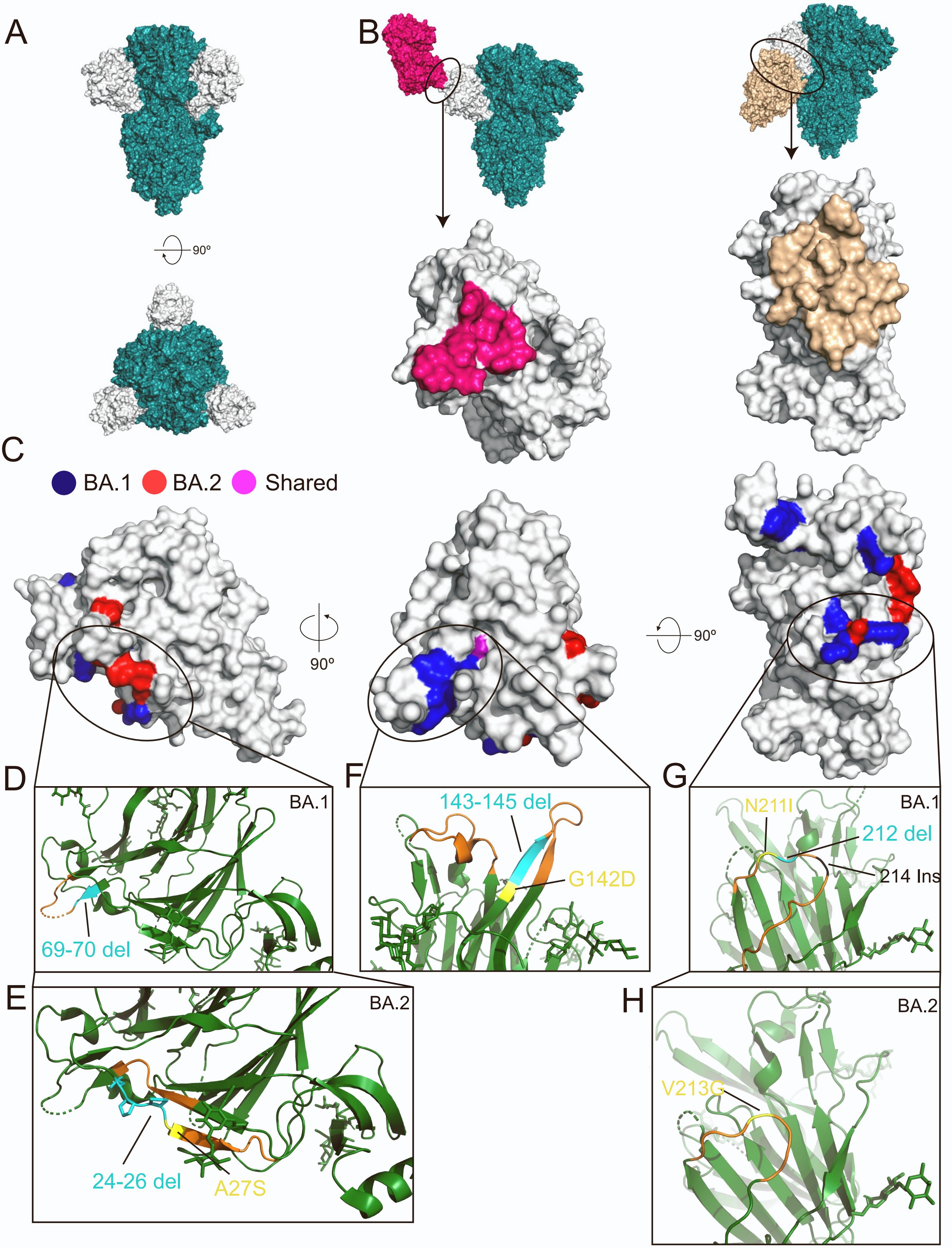
A
90º
B
C
● BA.1 ● BA.2 ● Shared
90º
90º
D
BA.1
69-70 del
E
BA.2
24-26 del
A27S
F
143-145 del
G142D
G
BA.1
N211I
212 del
214 Ins
H
BA.2
V213G

Data S6. Comparison of N-terminal domain (NTD) mutations between BA.1 and BA.2 lineages. Related to Figure 5. **A.** Surface view of the spike trimer, teal, with each NTD shown in white, side view and top view. **B.** Surface views of the spike, with Fab regions of NTD-targeted antibodies bound: DH1050.1, pink, and DH1052, gold, are both shown and the NTD is shown in isolation, with residues contacted by the antibodies highlighted with the same color. Only one NTD is colored white and only one antibody Fab are shown in these views. **C.** Three views of the wild-type NTD with residues mutated in the Omicron variants highlighted as follows: blue: BA.1, red: BA.2, magenta: shared in BA.1 and BA.2. **D-H.** Cartoon and Stick views showing mutated residues from areas highlighted in C. Color scheme for d-h is as follows: yellow: mutated residue, cyan: deleted residues, black: insertion site, orange: nearby residues/loop residues, other NTD residues: green. Models used: A: 7LAB, B: 7LCN (DH1050.1) and 7LAB (DH1052): C-H: 7LY3

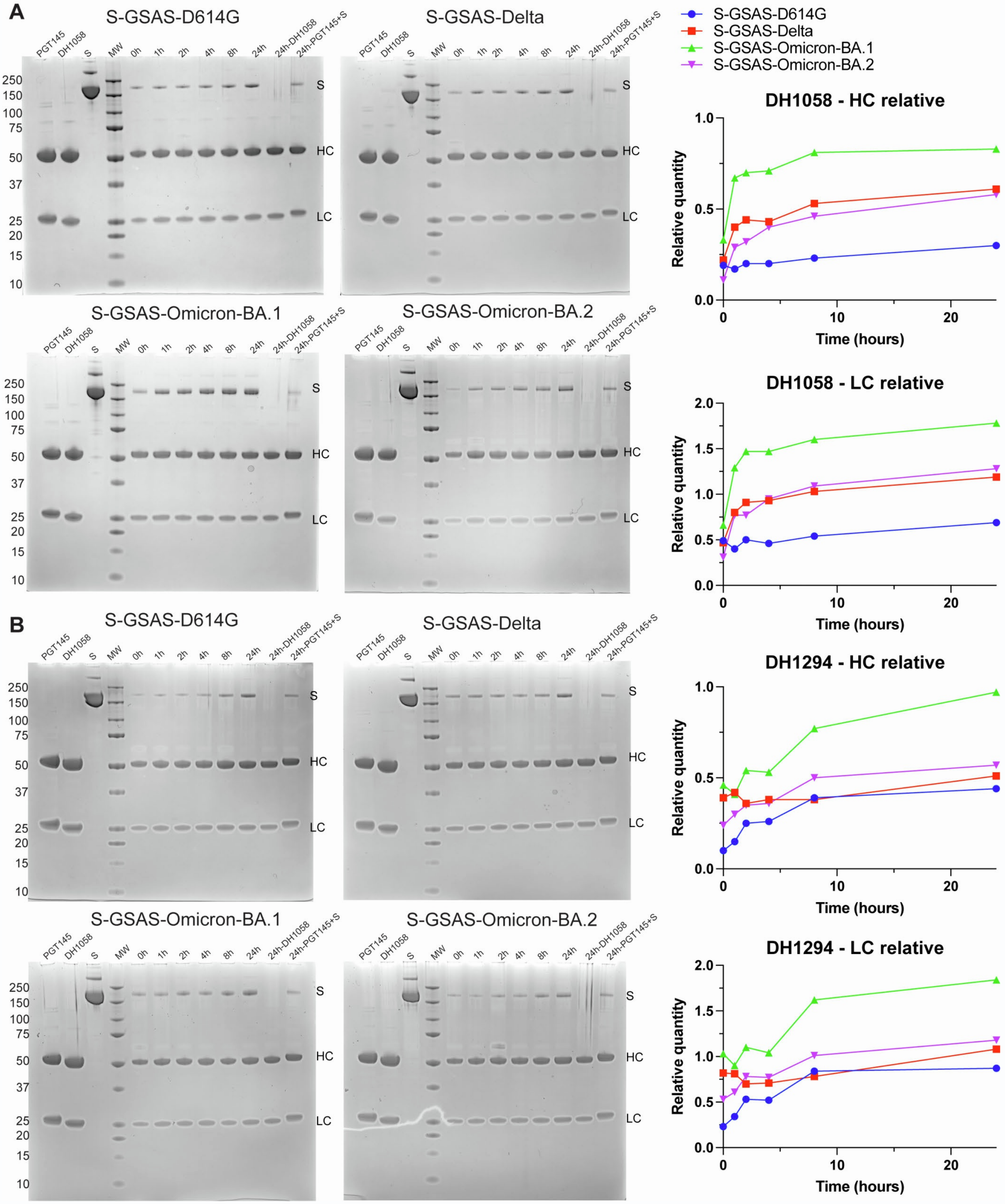
A
S-GSAS-D614G
S-GSAS-Delta
S-GSAS-Omicron-BA.1
S-GSAS-Omicron-BA.2
PGT145
DH1058
S
MW
0h
1h
2h
4h
8h
24h
24h-DH1058
24h-PGT145+S
250
150
100
75
50
37
25
20
15
10
S
HC
LC
B
S-GSAS-D614G
S-GSAS-Delta
S-GSAS-Omicron-BA.1
S-GSAS-Omicron-BA.2
DH1058 - HC relative
DH1058 - LC relative
DH1294 - HC relative
DH1294 - LC relative
Relative quantity
Time (hours)
0.0
0.5
1.0
1.5
2.0
0
10
20

Data S7. Time dependent exposure of fusion peptide (FP) to FP-directed antibodies, Related to Figure 7. A. Left. Reducing SDS-PAGE of immunoprecipitation of S-GSAS-D614G, S-GSAS-Delta, S-GSAS-Omicron-BA.1 and S-GSAS-Omicron-BA.2 using FP-directed antibody DH1058 bound to a Protein A coupled resin. Right. Intensity of the S protein band at each time point was normalized with the intensity of the heavy chain (HC, top) or light chain (LC, bottom) band. **B.** Same as **A.** but for antibody DH1294. Data shown are representative of at least two independent experiments.